POLITECNICO DI TORINO
Repository ISTITUZIONALE

A novel FEM approach for the analysis of Type-IV hydrogen storage tank based on the enhanced Refined Zigzag Theory

Original
A novel FEM approach for the analysis of Type-IV hydrogen storage tank based on the enhanced Refined Zigzag Theory / Valoriani, F., Credo, G., Gherlone, M.. - In: FINITE ELEMENTS IN ANALYSIS AND DESIGN. - ISSN 0168-874X. - ELETTRONICO. - 260:(2026). [10.1016/j.finel.2026.104607]

Availability:
This version is available at: 11583/3012757 since: 2026-07-06T11:40:32Z

Publisher:
Elsevier

Published
DOI:10.1016/j.finel.2026.104607

Terms of use:

This article is made available under terms and conditions as specified in the corresponding bibliographic description in the repository

Publisher copyright

(Article begins on next page)

19 November 2026

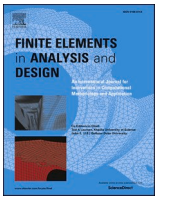
Finite Elements in Analysis and Design 260 (2026) 104607



Contents lists available at ScienceDirect

Finite Elements in Analysis & Design

journal homepage: www.elsevier.com/locate/finel



A novel FEM approach for the analysis of Type-IV hydrogen storage tank based on the enhanced Refined Zigzag Theory

Filippo Valoriani [a,*], Giuseppe Credo [b], Marco Gherlone [a]

[a] Politecnico di Torino, Department of Mechanical and Aerospace Engineering, Corso Duca degli Abruzzi 24, Torino, 10129, Italy
[b] DUMAREY Automotive Italia S.p.A, Department of Virtual Engineering and NVH, Corso Castelfidardo 36, Torino, 10129, Italy

ARTICLE INFO

Keywords:
Composite pressure vessel
Hydrogen
Enhanced-Refined Zigzag Theory
Layered structures
Finite elements

ABSTRACT

While high-pressure gas storage is the most practical method for hydrogen transport, it requires extreme internal pressures to compensate for the fuel's low volumetric energy density. Such operational demands lead to severe structural stresses, necessitating high-strength composite materials to achieve an optimal balance between safety and weight efficiency. Consequently, accurate displacement and stress analyses of these multilayered structures are vital for structural optimization. This paper presents a Finite Element (FE) formulation based on the enhanced-Refined Zigzag Theory (en-RZT), specifically tailored for composite pressure vessels. In particular, a quadrilateral flat shell finite element based on the en-RZT is formulated for the first time (ZZen-Q), enabling the analysis of complex, curved multilayered structures. Numerical benchmarks, including static and modal analyses of multilayered plates, cylinders, and tanks, are conducted to evaluate the accuracy and efficiency of the proposed ZZen-Q element against standard shell FE models and high-fidelity 3D FE models. The results demonstrate that ZZen-Q significantly outperform standard shell elements in accuracy with only a marginal increase in nodal degrees of freedom. Furthermore, while providing static and dynamic predictions comparable to high-fidelity 3D models, the en-RZT-based FE approach requires a substantially lower computational effort. These findings position the ZZen-Q shell elements as powerful tools for the preliminary design and optimization of hydrogen storage systems, facilitating rapid, high-performance design iterations prior to final validation.

1. Introduction

Hydrogen is increasingly recognized as an important player in the transition to sustainable power source [1], with applications ranging from transportation to industry and electric power generation [2]. Among the available storage methods, compressed hydrogen gas stored in Composite Overwrap Pressure Vessels (COPVs) is a practical and common storage solution for both aerospace [3] and automotive applications [4–7].

Type-IV COPVs, which combine a polymeric liner with a CFRP overwrap [8], have emerged as a leading solution due to their superior strength-to-weight ratio. These vessels are particularly effective in allowing the increasing of the internal pressure, thereby improving the volumetric density of the stored hydrogen. At present, the most common manufacturing technique for composite pressure vessel is filament winding, which enables high strength/stiffness to weight ratios and high fiber volume fractions [9,10].

* Corresponding author.
E-mail address: filippo.valoriani@polito.it (F. Valoriani).

https://doi.org/10.1016/j.finel.2026.104607
Received 17 April 2026; Received in revised form 8 June 2026; Accepted 28 June 2026
0168-874X/© 2026 The Author(s). Published by Elsevier B.V. This is an open access article under the CC BY license (http://creativecommons.org/licenses/by/4.0/).

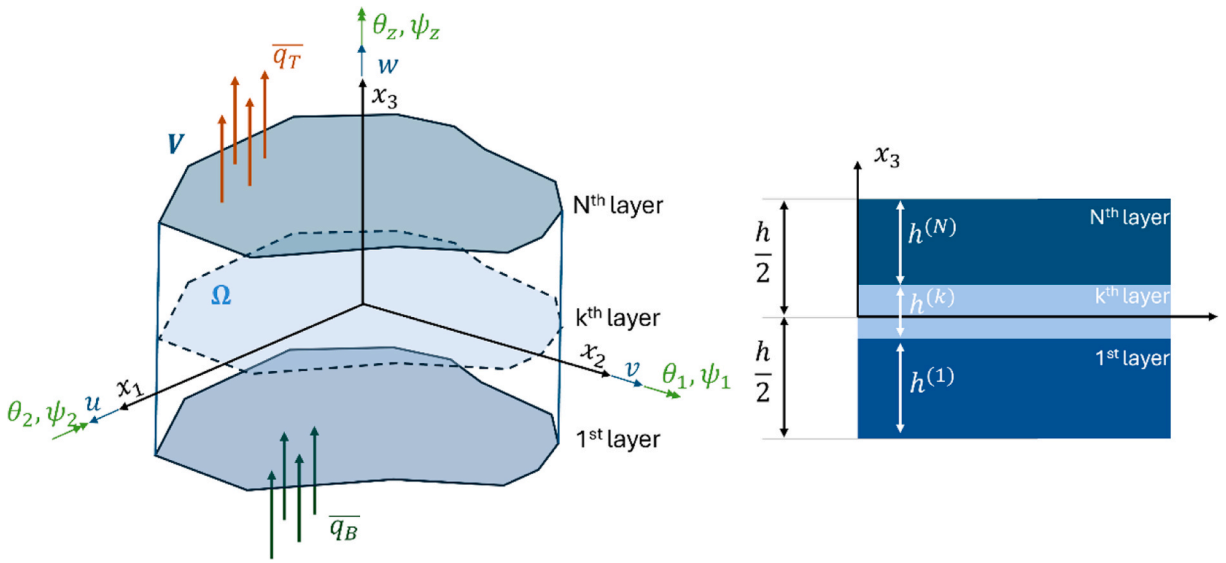


Fig. 1. Multilayered plate geometry, loads and notation.

The design of COPVs for hydrogen storage is further complicated by stringent standards such as UN regulation n. 134 [2019/795] [11] which impose mandatory burst, fatigue, and impact testing and require extensive numerical pre-screening before physical prototyping. Accurate finite element simulations [12,13] require high computational costs, particularly for resolving the complex through-the-thickness stress state under high pressure loading conditions. This cost becomes critical during the optimization phase, when iterative analyses are required for testing numerous configurations, stacking sequences, winding angles, and layer thicknesses. In particular, the computational cost of 3D, solid finite element models increases proportionally with the number of layers, because each lamina requires at least one through-the-thickness sub-division. Recent studies have attempted to mitigate this drawback through surrogate modeling approaches, such as kriging based metamodels [14] and deep neural networks [15], which approximate the structural response at a reduced computational effort. However, these approaches require a sufficiently large training dataset, typically generated from full 3D FE analyses. An alternative strategy is to adopt structurally precise yet computationally efficient FE formulations that preserve the physics of layered structures while substantially reducing the number of degrees of freedom. This is the approach pursued in the present work.

The traditional method for analyzing multilayered structures relies on kinematic assumptions that produce a displacement field. Equivalent Single Layer theories (ESL) are the ones where the displacement field assumptions are valid throughout the entire thickness. Among these, the most common are the Classical Lamination Theory [16] and the First-order Shear Deformation Theory (FSDT) [17,18]. These simple approaches are computationally affordable and provide accurate predictions of global quantities (deflection, natural frequencies, and buckling loads) for thin multilayered structures with reduced transverse anisotropy [19]. On the other hand, LayerWise theories (LW) assume displacement and stress fields separately for each layer [20], thus being able to more accurately reproduce local responses (including through-the-thickness distributions of strains and stresses) for highly anisotropic laminates but incurring in a large number of kinematic variables (that increase with the number of layers). An attempt to find a trade-off between high accuracy and low computational effort is represented by Zigzag Theories, whose origins can be traced back to Ref. [21], with subsequent important contributions from Refs. [22–24]. The basic idea of Zigzag Theories is to enrich the displacement field of ESL approaches with piecewise linear or cubic ("zigzag") enrichments, in particular for in-plane displacements, thus correctly modeling the thickness-normal distortion typical of multilayered structures. Moreover, the number of kinematic variables is reduced and kept constant when increasing the number of layers [23,24]. Developments within the Zigzag class of approaches have been proposed with the Refined Zigzag Theory (RZT) [25], that increased consistency and accuracy of response predictions at clamped edges [26,27] and numerical efficiency of related finite elements [28]. Improved performances in terms of stress field predictions, in particular for transverse shear components, have been obtained by developing special RZT formulations based on mixed variational approaches, as the Reissner's Mixed Variational Theorem [29] or the Hellinger Reissner principle [30]. Higher-order versions of RZT have also been proposed, with additional through-the-thickness contributions to both the in-plane and the transverse displacement components, thus allowing the modeling of transverse-stretching effects and leading to accurate predictions of the transverse normal stress [31,32]. Approaches that are both mixed and based on higher-order expansions of the displacement field are also available [33]. A recent further development of RZT models is the enhanced Refined Zigzag Theory (en-RZT) [34], able to take into account zigzag coupling effects exhibited by in-plane displacements in angle-ply stacking sequences (typical of pressurized vessels). In particular, in Ref. [34], it is shown that for lay-ups with orientation sequences as $[+\theta,-\theta]$, the original RZT can be very inaccurate, in some cases even leading to the vanishing of the zigzag enrichments, whereas en-RZT is able to preserve the zigzag effect.

Aim of the present study is to formulate and numerically validate an accurate and efficient FE approach for the linear static and free vibration analysis of COPVs based on the en-RZT. A flat shell element for curved structures based on the original RZT has already been

proposed [28], plate elements based on en-RZT for the analysis of flat structures have been formulated in Ref. [35]. In the present paper, for the first time, an en-RZT quadrilateral flat shell finite element is formulated (ZZen-Q) that can be used to model complex, curved multilayered structures. Since the main application field is of industrial interest, the assessment of ZZen-Q is performed by means of comparisons with two other approaches, available in FE commercial codes and representing standard levels of approximation within any industrial framework: (1) shell finite elements based on Mindlin's plate theory and (2) detailed FE models based on 3D elements. Future developments of the present effort will also include comparative studies with alternative methods, as those based on the solid-shell approach and applicable to thin and moderately thick structures [36].

The paper is organized as follows. The basic assumptions and equations of en-RZT are summarized in Section 2, then the ZZen-Q finite element is formulated in Section 3. Some numerical test cases related to multilayered square plates, sandwich cylinders and laminated tanks are then considered to assess the convergence behavior, the accuracy, and numerical efficiency of the ZZen-Q (Section 4). The proposed approach is found to be more accurate than standard, FSDT-based shell FE models with a negligible increase in terms of computational effort and, at the same time, to provide response predictions similar to those coming from high-fidelity 3D FE models but with much fewer nodal degrees of freedom.

2. Enhanced Refined Zigzag Theory

This Section briefly recalls the basic assumptions and definitions and the governing equations of the enhanced-Refined Zigzag Theory (en-RZT) for general multilayered plates [34].

Let us consider a plate made of N layers perfectly bonded to one another (Fig. 1). V is the plate volume, h is the total thickness and Ω is the reference surface chosen to be the middle plane of the laminate. The points of the plate are referred to an orthogonal Cartesian coordinate system $(\mathbf{x}, x_3)$, where the vector $\mathbf{x} \equiv (x_1, x_2)$ collects the in-plane coordinates belonging to the reference surface and x_3 represents the thickness coordinate ($x_3 \in [-h/2, +h/2]$). The plate is subjected to transverse distributed loads per unit area acting on the bottom and top surface, $\overline{q}_B(\mathbf{x};t)$ and $\overline{q}_T(\mathbf{x};t)$, respectively.

The symbol $\langle \cdot \rangle = \int_{-h/2}^{+h/2} \cdot \, dx_3$ is used to indicate integration over the whole laminate thickness while the superscript $(\cdot)^{(k)}$ is used to indicate quantities corresponding to the kth layer (k = 1, …,N). Moreover, the symbol $(\cdot)_{,i} = \partial(\cdot)/\partial x_i$ refers to the derivative of a function with respect to the x_i-coordinate and an over-dot indicates differentiation with respect to time.

2.1. Displacements, strains, stresses

The displacement field, assumed according to the enhanced Refined Zigzag Theory (en-RZT) [34], can be expressed as

$$\begin{aligned} U_1^{(k)}(\mathbf{x}, x_3; t) &= u_1(\mathbf{x};t) + x_3\theta_1(\mathbf{x};t) + \phi_{11}^{(k)}(x_3)\psi_1(\mathbf{x};t) + \phi_{12}^{(k)}(x_3)\psi_2(\mathbf{x};t) \\ U_2^{(k)}(\mathbf{x}, x_3; t) &= u_2(\mathbf{x};t) + x_3\theta_2(\mathbf{x};t) + \phi_{21}^{(k)}(x_3)\psi_1(\mathbf{x};t) + \phi_{22}^{(k)}(x_3)\psi_2(\mathbf{x};t) \\ U_3(\mathbf{x}, x_3; t) &= w(\mathbf{x};t) \end{aligned} \tag{1}$$

where $U_1^{(k)}, U_2^{(k)}$ and U_3 are the displacement components along (x_1, x_2, x_3), respectively. In matrix compact form, Eq. (1) can be re-written as

$$\boldsymbol{U}(\mathbf{x}, x_3; t) \equiv \begin{Bmatrix} \begin{Bmatrix} U_1^{(k)} \\ U_2^{(k)} \end{Bmatrix} \\ U_3 \end{Bmatrix} = \begin{bmatrix} \mathbf{I} & \mathbf{0} & x_3\mathbf{I} & \boldsymbol{\phi}^{(k)}(x_3) \\ \mathbf{0} & 1 & \mathbf{0} & \mathbf{0} \end{bmatrix} \begin{Bmatrix} \boldsymbol{u}(\mathbf{x};t) \\ w(\mathbf{x};t) \\ \boldsymbol{\theta}(\mathbf{x};t) \\ \boldsymbol{\psi}(\mathbf{x};t) \end{Bmatrix} \equiv \boldsymbol{Z}_u(x_3)\boldsymbol{g}(\mathbf{x};t) \tag{2}$$

where $\boldsymbol{g}$ is the vector of the seven kinematic variables: $\boldsymbol{u}^T \equiv \lfloor u_1 \quad u_2 \rfloor$ are the uniform displacement components along the x_1- and x_2- axis, respectively, w is the transverse deflection assumed to be constant along the thickness direction, $\boldsymbol{\theta}^T \equiv \lfloor \theta_1 \quad \theta_2 \rfloor$ are the bending rotations of the transverse normal around the positive x_2- axis and the negative x_1- axis, respectively, $\boldsymbol{\psi}^T \equiv \lfloor \psi_1 \quad \psi_2 \rfloor$ are the zigzag rotations around the positive x_2- and negative x_1- direction, respectively, and measure the magnitude of the zigzag effect, i.e., the distortion of the normal typical of multilayered structures. The through-the-thickness piecewise linear and continuous pattern of the normal distortion is modeled by the zigzag functions $(\phi_{11}^{(k)}, \phi_{12}^{(k)}, \phi_{21}^{(k)}, \phi_{22}^{(k)})$ which depend on the thickness and on the transformed transverse shear moduli of each layer. The zigzag functions are collected in the matrix

$$\boldsymbol{\phi}^{(k)}(x_3) \equiv \begin{bmatrix} \phi_{11}^{(k)}(x_3) & \phi_{12}^{(k)}(x_3) \\ \phi_{21}^{(k)}(x_3) & \phi_{22}^{(k)}(x_3) \end{bmatrix} \tag{3}$$

and are obtained as a result of the partial transverse shear stress continuity across the laminate interfaces and by enforcing their vanishing on the bottom and top laminate surfaces, $\boldsymbol{\phi}^{(1)}(x_3=-h/2)=\boldsymbol{\phi}^{(N)}(+h/2)=\mathbf{0}$ (refer to Ref. [34] for full details on the derivation). The off-diagonal zigzag functions ($\phi_{12}^{(k)},\phi_{21}^{(k)}$) vanish for cross-ply stacking sequences whereas they are present for general laminates, thus providing a fully coupled zigzag effect within the in-plane displacement components and leading to more accurate results with respect to the original Refined Zigzag Theory (RZT) that totally neglects these zigzag functions [34].

Assuming linear strain-displacement relations, the strain components are obtained as follows

$$\left\{\begin{array}{c}\boldsymbol{\varepsilon}_{\mathrm{p}}^{(k)}(\mathbf{x},x_3;t)\\ \boldsymbol{\gamma}_t^{(k)}(\mathbf{x},x_3;t)\end{array}\right\}\equiv\left\{\begin{array}{c}\left\{\begin{array}{c}\varepsilon_{11}^{(k)}\\ \varepsilon_{22}^{(k)}\\ \gamma_{12}^{(k)}\end{array}\right\}\\ \left\{\begin{array}{c}\gamma_{13}^{(k)}\\ \gamma_{23}^{(k)}\end{array}\right\}\end{array}\right\}=\left[\begin{array}{ccccc}\mathbf{I} & x_3\mathbf{I} & \boldsymbol{\Phi}^{(k)}(x_3) & \mathbf{0} & \mathbf{0}\\ \mathbf{0} & \mathbf{0} & \mathbf{0} & \mathbf{I} & \boldsymbol{\beta}^{(k)}(x_3)\end{array}\right]\left\{\begin{array}{c}\boldsymbol{\varepsilon}_m(\mathbf{x};t)\\ \boldsymbol{\varepsilon}_\theta(\mathbf{x};t)\\ \boldsymbol{\varepsilon}_\psi(\mathbf{x};t)\\ \boldsymbol{\gamma}(\mathbf{x};t)\\ \boldsymbol{\psi}(\mathbf{x};t)\end{array}\right\}\equiv\mathbf{Z}_e(x_3)\boldsymbol{e}(\mathbf{x};t) \tag{4}$$

where $\boldsymbol{e}$ is the vector collecting the strain measures (and the zigzag rotations $\boldsymbol{\psi}$)

$$\begin{gathered}\boldsymbol{\varepsilon}_m(\mathbf{x};t)\equiv\left\{\begin{array}{c}u_{1,1}(\mathbf{x};t)\\ u_{2,2}(\mathbf{x};t)\\ u_{1,2}(\mathbf{x};t)+u_{2,1}(\mathbf{x};t)\end{array}\right\},\boldsymbol{\varepsilon}_\theta(\mathbf{x};t)\equiv\left\{\begin{array}{c}\theta_{1,1}(\mathbf{x};t)\\ \theta_{2,2}(\mathbf{x};t)\\ \theta_{1,2}(\mathbf{x};t)+\theta_{2,1}(\mathbf{x};t)\end{array}\right\},\boldsymbol{\varepsilon}_\psi(\mathbf{x};t)\equiv\left\{\begin{array}{c}\psi_{1,1}(\mathbf{x};t)\\ \psi_{2,2}(\mathbf{x};t)\\ \psi_{1,2}(\mathbf{x};t)\\ \psi_{2,1}(\mathbf{x};t)\end{array}\right\}\\ \boldsymbol{\gamma}(\mathbf{x};t)\equiv\left\{\begin{array}{c}\gamma_1(\mathbf{x};t)\\ \gamma_2(\mathbf{x};t)\end{array}\right\}=\left\{\begin{array}{c}\theta_1(\mathbf{x};t)+w_{,1}(\mathbf{x};t)\\ \theta_2(\mathbf{x};t)+w_{,2}(\mathbf{x};t)\end{array}\right\}=\boldsymbol{\theta}(\mathbf{x};t)+\partial\mathbf{w}(\mathbf{x};t)\end{gathered} \tag{5}$$

and where

$$\begin{gathered}\boldsymbol{\Phi}^{(k)}(x_3)\equiv\left[\begin{array}{cccc}\phi_{11}^{(k)}(x_3) & 0 & 0 & \phi_{12}^{(k)}(x_3)\\ 0 & \phi_{22}^{(k)}(x_3) & \phi_{21}^{(k)}(x_3) & 0\\ \phi_{21}^{(k)}(x_3) & \phi_{12}^{(k)}(x_3) & \phi_{11}^{(k)}(x_3) & \phi_{22}^{(k)}(x_3)\end{array}\right]\\ \boldsymbol{\beta}^{(k)}(x_3)\equiv\frac{\partial\boldsymbol{\phi}^{(k)}(x_3)}{\partial x_3}\end{gathered} \tag{6}$$

The material of each layer is assumed to be linear, elastic and orthotropic, with a plane of symmetry parallel to the laminate reference surface. Assuming the transverse normal stress to be negligible, $\sigma_{33}=0$, the in-plane and transverse shear stress components, ${\boldsymbol{\sigma}_p^{(k)}}^T(\mathbf{x},x_3;t)\equiv\left\lfloor\sigma_{11}^{(k)}\quad\sigma_{22}^{(k)}\quad\tau_{12}^{(k)}\right\rfloor$ and ${\boldsymbol{\tau}_t^{(k)}}^T(\mathbf{x},x_3;t)\equiv\left\lfloor\tau_{13}^{(k)}\quad\tau_{23}^{(k)}\right\rfloor$, respectively, can be calculated as follows

$$\begin{aligned}\boldsymbol{\sigma}_p^{(k)}(\mathbf{x},x_3;t)&=\mathbf{Q}_p^{(k)}\boldsymbol{\varepsilon}_p^{(k)}(\mathbf{x},x_3;t)\\ \boldsymbol{\tau}_t^{(k)}(\mathbf{x},x_3;t)&=\mathbf{Q}_t^{(k)}\boldsymbol{\gamma}_t^{(k)}(\mathbf{x},x_3;t)\end{aligned} \tag{7}$$

where $\mathbf{Q}_p^{(k)}=\left[Q_{ij}^{(k)}\right]$ $(i,j=1,2,6)$ and $\mathbf{Q}_t^{(k)}=\left[Q_{\alpha\beta}^{(k)}\right]$ $(\alpha,\beta=4,5)$ are the in-plane reduced and transverse shear elastic stiffness coefficients of the kth layer expressed in the plate axes, respectively.

2.2. Governing equations

The governing equations for en-RZT can be easily obtained using the d'Alembert Principle involving the virtual variation of the strain energy, δE_s, the virtual work of inertia forces, δW_{i}, and the virtual work of external loads, δW_{e}

$$\delta E_s=\delta W_i+\delta W_e \tag{8}$$

The virtual variation of the strain energy may be expressed as

$$\delta E_s \equiv \int_V \left(\delta \boldsymbol{\varepsilon}_p^{(k)^T} \boldsymbol{\sigma}_p^{(k)} + \delta \boldsymbol{\gamma}_t^{(k)^T} \boldsymbol{\tau}_t^{(k)} \right) dV = \int_\Omega \langle \delta \boldsymbol{\varepsilon}_p^{(k)^T} \boldsymbol{\sigma}_p^{(k)} + \delta \boldsymbol{\gamma}_t^{(k)^T} \boldsymbol{\tau}_t^{(k)} \rangle d\Omega \tag{9}$$

Substituting Eqs. (4) and (7) into Eq. (9) and integrating over the laminate thickness, yields

$$\delta E_s = \int_\Omega \delta \boldsymbol{e}^T \boldsymbol{k} \boldsymbol{e} d\Omega \tag{10}$$

where $\boldsymbol{k}$ is a matrix containing the stiffness coefficients of the laminate based on the en-RZT assumptions (refer to Appendix A for the detailed expression).

The virtual work of inertia forces is

$$\delta W_{\mathrm{i}} \equiv -\int_V \delta \boldsymbol{U}^T \ddot{\boldsymbol{U}} \rho^{(k)}(x_3) dV = -\int_\Omega \langle \delta \boldsymbol{U}^T \ddot{\boldsymbol{U}} \rho^{(k)}(x_3) \rangle d\Omega \tag{11}$$

where $\rho^{(k)}(x_3)$ is the material mass density. Substituting Eq. (2) into Eq. (11) and integrating over the laminate thickness, leads to the following expression

$$\delta W_{\mathrm{i}} = -\int_\Omega \delta \boldsymbol{g}^T \boldsymbol{m} \ddot{\boldsymbol{g}} d\Omega \tag{12}$$

where $\boldsymbol{m}$ collects the inertia coefficients of the laminate for en-RZT (refer to Appendix A for the detailed expression).

The virtual work of external forces is

$$\delta W_{\mathrm{e}} \equiv \int_\Omega \delta w \overline{q} d\Omega \tag{13}$$

where $\overline{q} \equiv \overline{q}_B + \overline{q}_T$ is the total transverse distributed load.

The Euler-Lagrange equations of motion for en-RZT and the corresponding set of consistent boundary conditions can be obtained from the d'Alembert's principle, Eq. (8), and by using Eqs. (10), (12) and (13) (refer to [37] for the details of the derivation and for the full set of equations and boundary conditions in the case of static problems).

3. Finite element formulation

The formulation of a flat shell finite element can be obtained by introducing an approximation of the kinematic variables $\boldsymbol{g}$ and of their derivatives $\boldsymbol{e}$ in the expressions of the virtual variation of strain energy and of the virtual work of inertia and external forces (Eqs. (10), (12) and (13)) and by using the d'Alembert's principle, Eq. (8). Since $\boldsymbol{e}$ contains derivatives not exceeding the first order, it is possible to use C^0-continuous shape functions. The derivation of the shape functions follows what was proposed by Tessler for FSDT-based shell elements in Ref. [38] and was then extended to the {1,2}-theory in Ref. [39] and to RZT in Ref. [28]. What is summarized below is the main procedure for quadrilateral elements (for further details, please refer to Ref. [28]).

- The in-plane displacements and the transverse deflection are approximated with quadratic shape functions associated with nodes located at the corners and at the mid-points of the element edges. Both bending and zigzag rotations are approximated with linear shape functions and nodal degrees of freedom related to corner nodes only. The "drilling rotation" θ_z, defined around the normal to the element surface, is also introduced and linearly interpolated in order to obtain a fully compatible displacement field at the interface between non co-planar adjacent elements for modelling curved and built-up structures. The different degrees of approximation for displacements and rotations (according to the anisoparametric interpolation scheme [40]) are used to alleviate shear-locking.
- Constraining conditions are applied on the edges of the element considered as RZT-based beam finite elements [28]. It has to be noted that no difference appears between RZT and en-RZT when modeling a beam in cylindrical bending, thus the "superposition" of RZT beam finite elements on the edges of en-RZT shell finite elements is consistent and the same constraining conditions developed in Ref. [28] can be adopted. These conditions allows condensing out the displacement degrees of freedom associated with the mid-edge nodes.

The resulting approximation for the three displacements, three rotations (bending and drilling) and two zigzag rotations within quadrilateral elements with corner nodes only is obtained as follows

$$
\begin{aligned}
u(\boldsymbol{x},t) &= \sum_{i=1}^{4} u_i(t)L_i(\boldsymbol{x}) + \sum_{i=1}^{4} \theta_{zi}(t)Q_{2i}(\boldsymbol{x}) \\
v(\boldsymbol{x},t) &= \sum_{i=1}^{4} v_i(t)L_i(\boldsymbol{x}) - \sum_{i=1}^{4} \theta_{zi}(t)Q_{1i}(\boldsymbol{x}) \\
w(\boldsymbol{x},t) &= \sum_{i=1}^{4} w_i(t)L_i(\boldsymbol{x}) + \sum_{i=1}^{4} (\theta_{1i}(t) - \psi_{1i}(t))Q_{1i}(\boldsymbol{x}) + \sum_{i=1}^{4} (\theta_{2i}(t) - \psi_{2i}(t))Q_{2i}(\boldsymbol{x}) \\
\theta_1(\boldsymbol{x},t) &= \sum_{i=1}^{4} \theta_{1i}(t)L_i(\boldsymbol{x}) \\
\theta_2(\boldsymbol{x},t) &= \sum_{i=1}^{4} \theta_{2i}(t)L_i(\boldsymbol{x}) \\
\theta_z(\boldsymbol{x},t) &= \sum_{i=1}^{4} \theta_{zi}(t)L_i(\boldsymbol{x}) \\
\psi_1(\boldsymbol{x},t) &= \sum_{i=1}^{4} \psi_{1i}(t)L_i(\boldsymbol{x}) \\
\psi_2(\boldsymbol{x},t) &= \sum_{i=1}^{4} \psi_{2i}(t)L_i(\boldsymbol{x})
\end{aligned}
\tag{14}
$$

where $L_i(\mathbf{x})$, $Q_{1i}(\mathbf{x})$ and $Q_{2i}(\mathbf{x})$ are functions defined in Appendix B, and the following nodal degrees of freedom are considered

$$
q^e \equiv [\,[u_i] \quad [v_i] \quad [w_i] \quad [\theta_{1i}] \quad [\theta_{2i}] \quad [\theta_{zi}] \quad [\psi_{1i}] \quad [\psi_{2i}]\,]^T, i = 1, \ldots, 4 \tag{15}
$$

Starting from Eq. (15), it is possible to express both vectors of kinematic variables and of strain measures, $\boldsymbol{g}$ and $\boldsymbol{e}$ respectively (Eqs. (2) and (4)), in terms of the nodal degrees of freedom $\mathbf{q}^e$

$$
\boldsymbol{g}(\mathbf{x},t) = \mathbf{N}(\mathbf{x})\mathbf{q}^e(t) \tag{16}
$$

$$
\boldsymbol{e}(\mathbf{x},t) = \mathbf{S}(\mathbf{x})\mathbf{q}^e(t) \tag{17}
$$

where $\mathbf{N}(\mathbf{x})$ and $\mathbf{S}(\mathbf{x})$ are shape function matrices defined in Appendix B.

Using the finite element approximation (Eqs. (14), (16) and (17)) into the d'Alembert Principle (Eq. (8)) where the single terms are expressed as in Eqs. (10), (12) and (13), yields the equation of motion at the single finite element level

$$
\boldsymbol{M}^e\ddot{\boldsymbol{q}}^e + \boldsymbol{K}^e\boldsymbol{q}^e = \boldsymbol{f}^e \tag{18}
$$

where

$$
\mathbf{M}^e \equiv \int_{\Omega^e} \mathbf{N}^T \boldsymbol{m} \mathbf{N} d\Omega \tag{19}
$$

$$
\mathbf{K}^e \equiv \int_{\Omega^e} \mathbf{S}^T \boldsymbol{k} \mathbf{S} d\Omega \tag{20}
$$

$$
\mathbf{f}^e \equiv \int_{\Omega^e} \mathbf{N}_w^T \bar{q} d\Omega \tag{21}
$$

with $\mathbf{N}_w$ being the third row of matrix $\mathbf{N}$ (Appendix B), such that $w(\mathbf{x},t) = \mathbf{N}_w(\mathbf{x})\mathbf{q}^e(t)$, and Ω^e being the element area.

In order to have a formulation that allows the connection between non co-planar adjacent finite elements (as required when analyzing curved or built-up structures), the transversal component of the zigzag rotation, ψ_z, must be added in order to form, together with zigzag rotations ψ_1 and ψ_2, the complete set of zigzag rotation components in a three-dimensional reference system. This requirement is based on the equivalent and well-established introduction of the drilling rotation, θ_z, within shell elements that already have the bending rotations, θ_1 and θ_2, as degrees of freedom. This additional zigzag rotation is linearly interpolated within the element, thus leading to one additional degree of freedom per node, ψ_{zi}

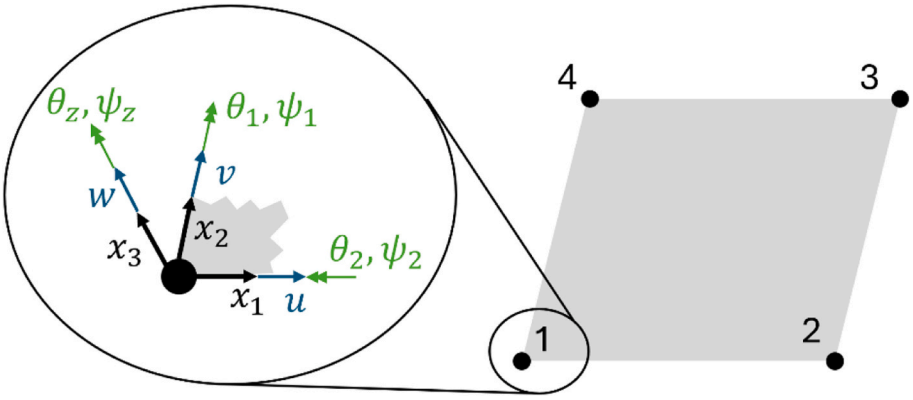


Fig. 2. Topology and nodal degrees of freedom for a quadrilateral element.

Table 1
Material properties. Elastic moduli are reported in [GPa], mass densities in [kg/m^3].

Material name	E_1	$E_2 = E_3$	$\nu_{12} = \nu_{13}$	ν_{23}	$G_{12} = G_{13}$	G_{23}	ρ
A	175	7	0.25	0.25	3.5	1.4	1000
B	15	1	0.3	0.35	0.5	0.35	1000
C	135	9.66	0.25	0.41	5.86	3.46	1800
Al	69		0.3				2700
Foam (isotropic)	0.9		0.46				950

Table 2
Laminate stacking sequences.

Laminate ID	Normalized thickness h^k/h	Lamina materials	Lamina orientations [°]
L0	[0.3333/0.3333/0.3333]	[A/A/A]	[0/90/0]
L1	[0.5/0.5]	[A/A]	[−15/+15]
L2	$[0.1/0.1]_5$	$[B/B]_5$	$[-45/+45]_5$
Laminate ID	**Thickness h^k [mm]**	**Lamina materials**	**Lamina orientations [°]**
L3	[1.5/2/1.5]	[Al/Foam/Al]	[0/0/0]
L4	[1/1/0.5/0.5/0.5/0.5/0.5/0.5]	$[C]_8$	[89/88/60/−60/10/−10/8/−8]

$$\psi_z(\boldsymbol{x}, t) = \sum_{i=1}^{4} \psi_{zi}(t) L_i(\boldsymbol{x}) \tag{22}$$

The expanded vector of degrees of freedom is defined as

$$\widetilde{\mathbf{q}}^e \equiv [\,[u_i] \quad [v_i] \quad [w_i] \quad [\theta_{1i}] \quad [\theta_{2i}] \quad [\theta_{zi}] \quad [\psi_{1i}] \quad [\psi_{2i}] \quad [\psi_{zi}]\,]^T \tag{23}$$

The topology and the degrees of freedom for a quadrilateral element are shown in Fig. 2.

The mass matrix, stiffness matrix and external force vector (Eqs. (19)–(21)) are also expanded with zero coefficients, thus obtaining $\widetilde{\boldsymbol{M}}^e$, $\widetilde{\boldsymbol{K}}^e$ and $\widetilde{\boldsymbol{f}}^e$. The stiffness matrix is then corrected with two additional terms as follows [28]

$$\widetilde{\boldsymbol{K}}^e = \widetilde{\boldsymbol{K}}^e + \lambda_\psi C_\psi \widetilde{\boldsymbol{K}}^e_\psi + \lambda_\theta C_\theta \widetilde{\boldsymbol{K}}^e_\theta \tag{24}$$

where:

- the first term is used to introduce the artificial stiffness coefficients corresponding to ψ_z according to a penalty approach, λ_ψ is a penalty parameter whose value can be set to 10^{-5} (refer to the results in Section 4.2), C_ψ is a dimensional stiffness coefficient, and $\widetilde{\mathbf{K}}^e_\psi$ is a matrix whose definitions can be found in Appendix C;
- the second term is a stabilization matrix used to inhibit the zero-energy spurious modes that may arise when all the drilling rotations θ_z assume the same value, λ_θ is a penalty parameter with recommended value 10^{-5} (refer to the results in Section 4.2), C_θ and $\widetilde{\mathbf{K}}^e_\theta$ are defined in Appendix C.

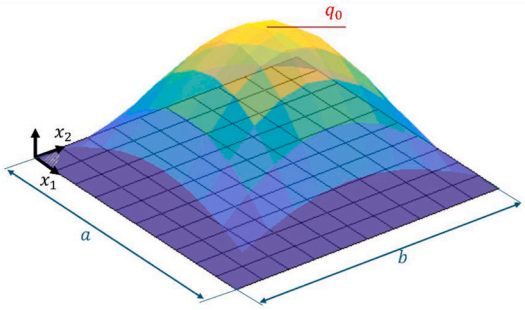


Fig. 3. Square plate with transverse bi-sinusoidal load.

Table 3
Simply-supported boundary conditions.

Boundary conditions	Edge's nodal DOF restrained
Simply supported (SS1) for L0	$@\ x_1 = 0, a : u_2 = w = \theta_2 = \psi_2 = 0$ $@\ x_2 = 0, b : u_1 = w = \theta_1 = \psi_1 = 0$
Simply supported (SS2) for L1, L2	$@\ x_1 = 0, a : u_1 = w = \theta_2 = \psi_2 = 0$ $@\ x_2 = 0, b : u_2 = w = \theta_1 = \psi_1 = 0$

Table 4
Exact en-RZT results for simply supported square plates.

$\frac{a}{h}$	$\overline{w}$		$\bar{f}$	
	L0	L1	L0	L2
10	0.7402	0.7821	1.8407	2.2085
10^2	0.4346	0.6221	2.4141	2.5389
10^3	0.4313	0.6205	2.4235	2.5431

The final system of motion equations in terms of the expanded vector of degrees of freedom is therefore

$$\widetilde{\boldsymbol{M}}^e \ddot{\widetilde{\boldsymbol{q}}}^e + \widetilde{\mathbf{K}}^e \widetilde{\boldsymbol{q}}^e = \widetilde{\mathbf{f}}^e \tag{25}$$

The transformation from the element-local coordinate system (and related nodal degrees of freedom, $\widetilde{\boldsymbol{q}}^e$) to the structure-global one is described in Appendix D.

4. Numerical results

In this section, we investigate the numerical performances of the developed finite element, denoted as ZZen-Q, by assessing its convergence behavior, accuracy, and computational cost while considering the static response and the free vibrations of simple rectangular plates, sandwich cylinders and multilayered pressure tanks. Table 1 and Table 2 show the material properties and stacking sequences considered for this numerical investigation.

Since the proposed ZZen-Q is a flat shell element, two-dimensional meshes used to discretize curved surfaces are created in such a way that any quadrilateral element is flat. Moreover, pressure loads are modeled within any shell element considering a transverse distributed load $\overline{q}$ that is locally perpendicular to the reference surface of that element.

4.1. Convergence analysis – multilayered square plates

Hereafter, we assess the convergence behavior of the proposed ZZen-Q finite element by comparing its response predictions with two sets of en-RZT exact results related to static and modal analyses.

This study considers square plates (edge length $a = b$, span-to-thickness ratio a/h ranging from 10 to 10^3), with cross-ply and anti-symmetric angle-ply stacking sequences (L0, L1 and L2, Table 2), simply supported along all their edges. For the static analysis, a bi-sinusoidal transverse load pressure $\overline{q_0}$ with maximum intensity q_0 is applied, Fig. 3.

$$\overline{q_0}(x_1, x_2) = q_0 \sin\left(\pi \frac{x_1}{a}\right) \sin\left(\pi \frac{x_2}{b}\right) \tag{26}$$

The simply-supported boundary conditions slightly changes depending on the stacking sequence in order to enable obtaining exact en-RZT solutions (refer to Table 3 and [10]).

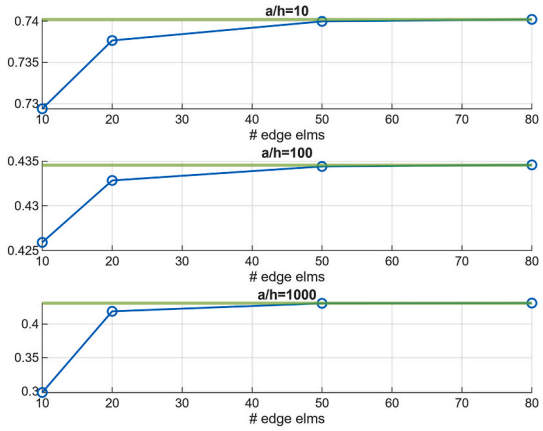


Fig. 4. ZZen-Q FE solution vs en-RZT exact solution convergence, L0 plate, non-dimensional maximum deflection $\overline{w}$.

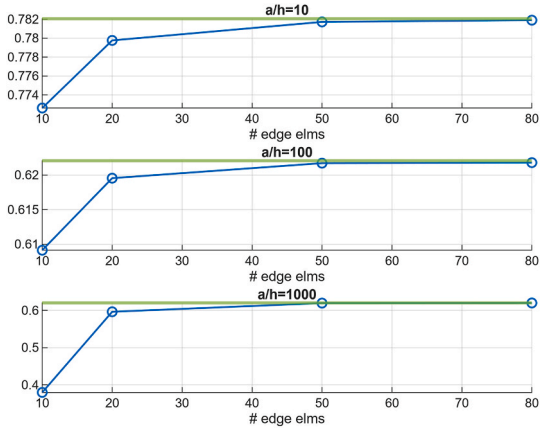


Fig. 5. ZZen-Q FE solution vs en-RZT exact solution convergence, L1 plate, non-dimensional maximum deflection $\overline{w}$.

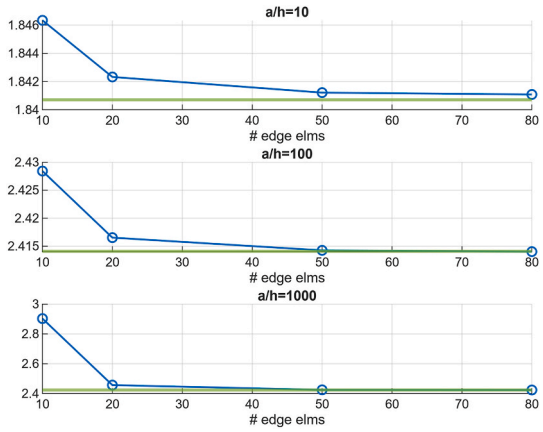


Fig. 6. ZZen-Q FE solution vs en-RZT exact solution convergence, L0 plate, non-dimensional fundamental frequency $\overline{f}$.

The reference, exact en-RZT results for the considered case studies (maximum deflection at the plate center, $w(x_1 = a/2, x_2 = a/2)$, and fundamental frequency, f), are obtained according to the usual Navier-type solution [35] and reported in Table 4 in non-dimensional form

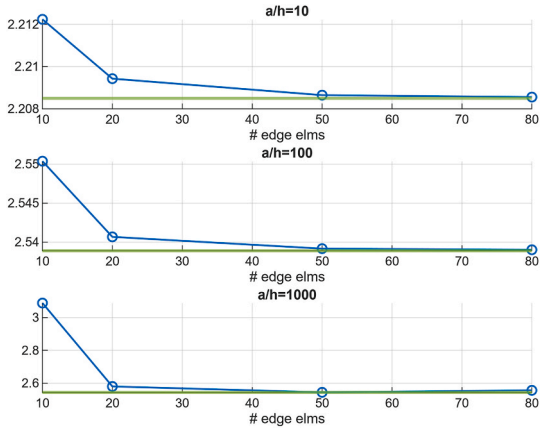


Fig. 7. ZZen-Q FE solution vs en-RZT exact solution convergence, L2 plate, non-dimensional fundamental frequency $\bar{f}$.

Table 5
Mesh properties for the cylinder problem. The 10 elements along the thickness of the cylinder for the HEXA20 model are distributed as follows: 3 per each external physical layer and 4 within the core.

Model	Elements along the length	Elements along the circumference	Through-the-thickness elements	Elements	Total nodes	Total dofs
ZZen-Q	18	79	1	1422	1501	13509
QUAD4	18	79	1	1422	1501	9006
HEXA20	56	258	10	144′480	629′520	1′888′560

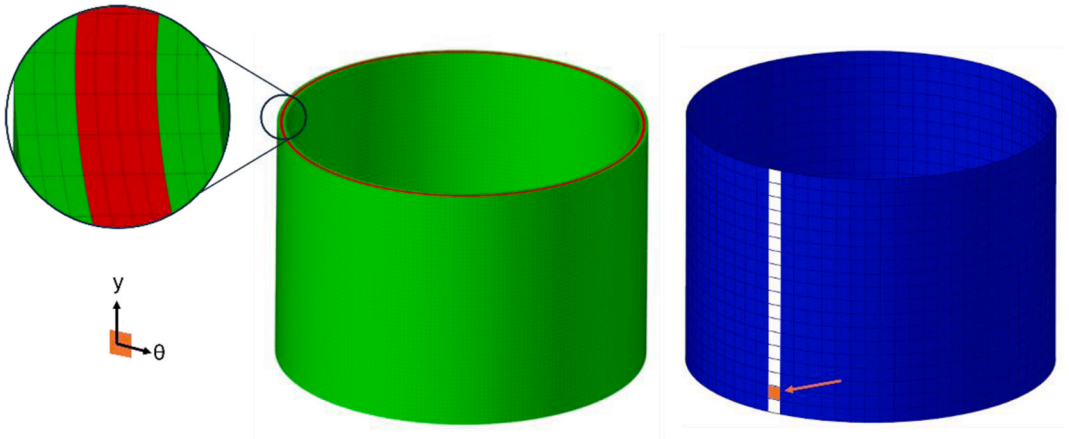


Fig. 8. Mesh schemes adopted for the cylinder problem: on the left, 3D HEXA20 mesh, on the right, 2D mesh for both ZZen-Q and QUAD4 models (white elements are those considered for the results shown in Figs. 10 and 11, the orange element is considered for the through-the-thickness distributions represented in Figs. 12 and 13). (For interpretation of the references to colour in this figure legend, the reader is referred to the Web version of this article.)

$$\overline{w} = w(x_1 = a/2, x_2 = a/2) \cdot 100 \frac{h^3 E_2^{(1)}}{q_0 a^4} \quad \bar{f} = f \cdot \frac{a^2}{h} \sqrt{\frac{\rho^{(1)}}{E_2^{(1)}}} \tag{27}$$

Fig. 4, Fig. 5, Fig. 6 and Fig. 7 demonstrate the convergence behavior of the ZZen-Q finite element analysis with respect to the exact en-RZT solution when increasing the mesh density (number of edge element subdivisions). At first, the convergence trend is consistent (from below, for the static problem, and from above, for the free vibration analysis). Moreover, even using a coarse mesh, the accuracy of the FE results is excellent (less than 3% error by means of a 20 x 20 mesh).

4.2. Accuracy and computational cost – sandwich cylinder

Aim of this section is to compare the proposed ZZen-Q solution with the FSDT-based QUAD4 (MSC/NASTRAN) and high-fidelity,

Table 6
Cylinder natural frequencies as computed with the 3D HEXA20 FE model and percent errors of the 2D FE models (including the average and the maximum absolute percent error).

	f_1, f_2	f_3, f_4	f_5, f_6	f_7, f_8	f_9, f_{10}	avg(|.|)	max(|.|)
HEXA20 [Hz]	1455	1814	1818	2494	3122	\	\
QUAD4 [%]	1.99	2.92	0.88	3.81	−0.26	1.97	3.81
ZZen-Q ($\lambda = \lambda_\psi = \lambda_\theta$) [%]							
λ = 0.0E+00	0.12	1.15	0.97	1.08	5.67	1.80	5.67
λ = 1.0E-01	−0.39	0.49	−1.24	0.84	−1.29	0.85	1.29
λ = 1.0E-02	−0.10	−0.06	−0.26	−0.41	−0.07	0.18	0.41
λ = 1.0E-03	0.00	−0.02	−0.17	−0.36	−0.02	0.11	0.36
λ = 1.0E-04	0.08	0.00	−0.12	−0.33	−0.01	0.11	0.33
λ = 1.0E-05	0.09	0.01	−0.11	−0.33	−0.01	0.11	0.33
λ = 1.0E-06	0.09	0.01	−0.11	−0.33	−0.01	0.11	0.33

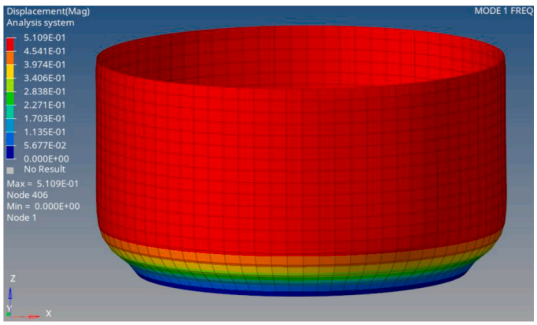


Fig. 9. Deformed shape of the sandwich cylinder subjected to a uniform internal pressure as obtained by the ZZen-Q model (the scale of the representation is magnified).

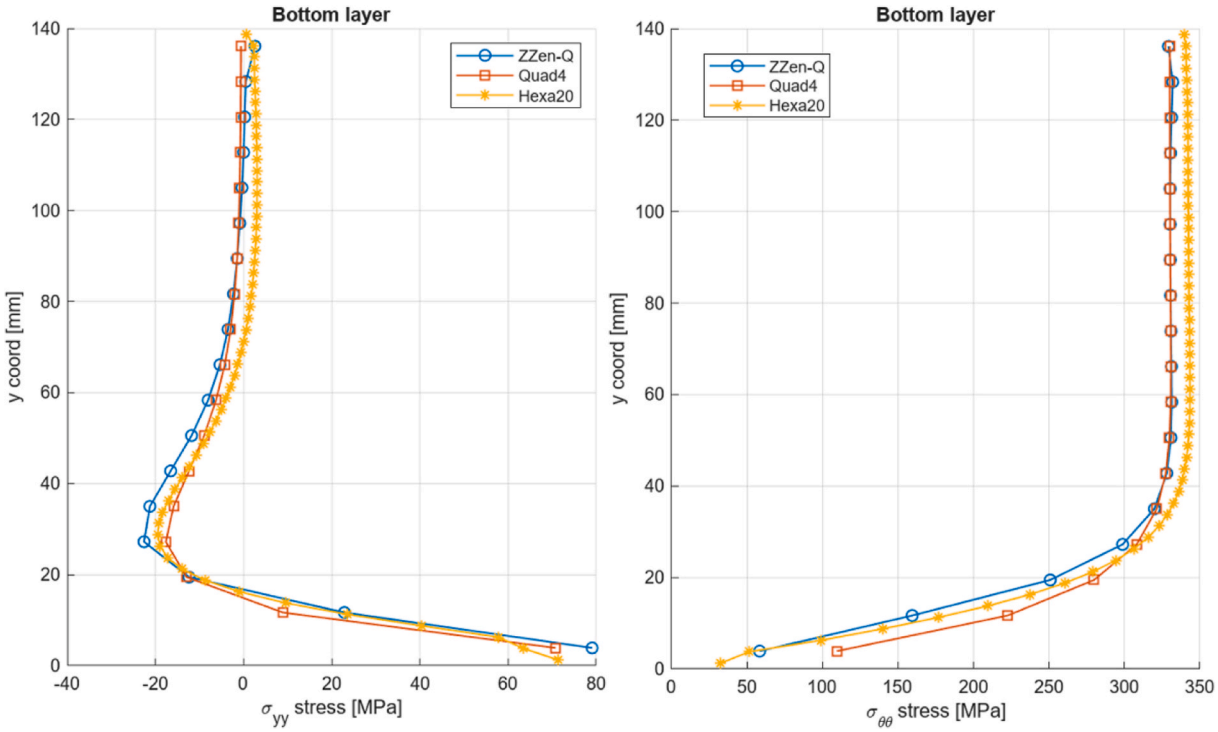


Fig. 10. Stress in θ and y directions in the bottom layer of the clamped cylinder subjected to internal pressure (white elements in Fig. 8).

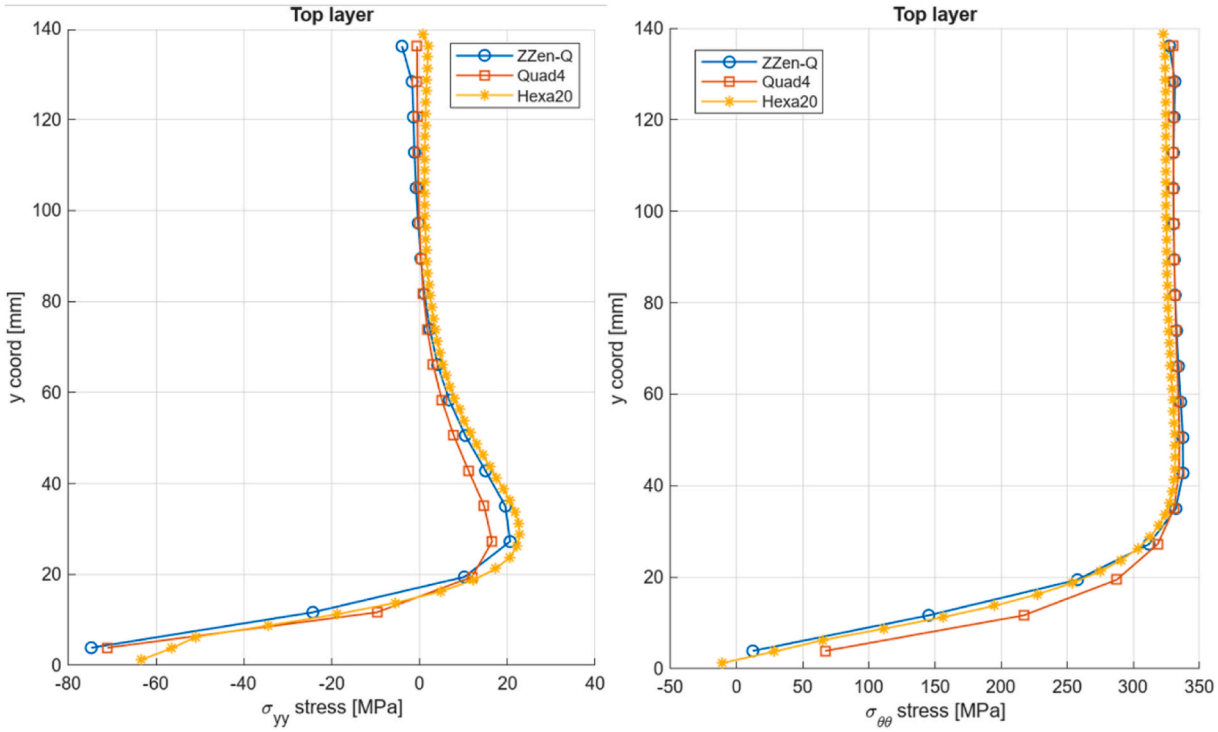


Fig. 11. Stress in θ and y directions in the top layer of the clamped cylinder subjected to internal pressure (white elements in Fig. 8).

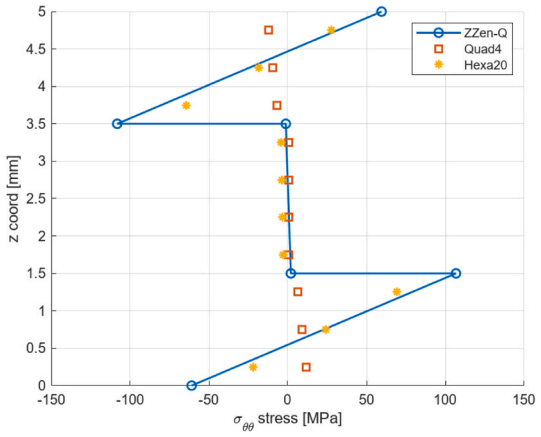


Fig. 12. Through-the-thickness distribution of the circumferential stress for the clamped cylinder subjected to internal pressure (orange elements in Fig. 8). (For interpretation of the references to colour in this figure legend, the reader is referred to the Web version of this article.)

3D HEXA20 model (MSC/NASTRAN) when curvature effects are involved. Moreover, a sensitivity analysis is performed on the effect of the penalty parameters, λ_θ and λ_ψ (refer to Eq. (24)), to assess their importance.

Let us consider a cylinder with internal radius 100 mm and length 140 mm, made of a sandwich-like lay-up (L3, refer to Table 2), clamped at the bottom circular edge. Details on the mesh for the ZZen-Q, QUAD4 and HEXA20 models are reported in Table 5 and shown in Fig. 8.

All degrees of freedom belonging to the clamped edge are constrained, whether they are displacements only (as in the 3D FE model) or both displacements and rotations (as in the 2D FE models).

Table 6 reports the first ten natural frequencies as obtained by reference [3D] HEXA20 model (modes are organized in couples due to the symmetry of the problem), the percent errors of the 2D FE models for each mode, the average and the maximum percent error over the modes. ZZen-Q results are obtained for different values of λ_θ and λ_ψ, including the case where no correction is applied ($\lambda_\theta = 0$ and $\lambda_\psi = 0$). In the latter condition, ZZen-Q is accurate but, starting from modes 9 and 10, a percent error higher than 5% is experienced. When implementing the correction according to Eq. (24), the trend of the percent errors show stable and more accurate results

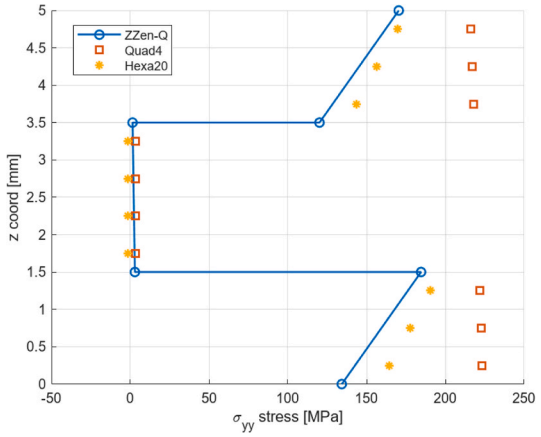


Fig. 13. Through-the-thickness distribution of the axial stress for the clamped cylinder subjected to internal pressure (orange elements in Fig. 8). (For interpretation of the references to colour in this figure legend, the reader is referred to the Web version of this article.)

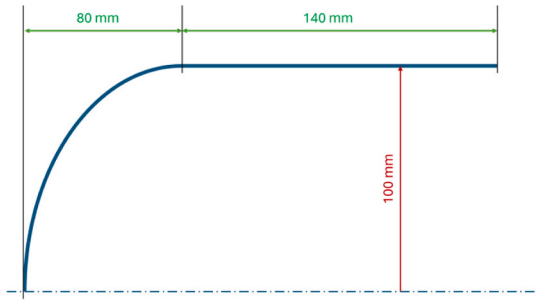


Fig. 14. Internal liner with elliptical dome dimensions (half of the tank is represented).

within the range $\lambda_\theta = \lambda_\psi = (10^{-6}, 10^{-4})$, thus the choice $\lambda_\theta = \lambda_\psi = 10^{-5}$ can be considered as a general recommendation (and has been adopted for the other numerical examples). The predictions obtained with QUAD4 elements can be considered accurate but some natural frequencies also experience errors over 3%, whereas ZZen-Q is able to keep the error below 1% ($\lambda_\theta = \lambda_\psi = 10^{-5}$) for the considered modes. This is achieved with a 2D ZZen-Q model slightly more computational demanding than the QUAD4 model (same number of elements, some more nodal degrees of freedom) but by far less computational demanding than the HEXA20 model.

The same cylinder is subjected to an internal uniform pressure of 10 MPa, thus experiencing a deformed shape as shown in Fig. 9. Figs. 10 and 11 show the distribution of the circumferential stress, $\sigma_{\theta\theta}$, and of the axial stress, σ_{yy}, computed by the three models along a row of elements (highlighted in white in Fig. 8). In particular, values of the two stresses are calculated at the centroid of the elements and at the mid-thickness of both the bottom-internal and of the top-external layer.

Figs. 10 and 11 reveal two separate stress regimes within the pressurized cylinder. One regime far from the clamped circumference, with predominant circumferential stress and negligible axial stress and with ZZen-Q and QUAD4 similarly accurate if compared with the HEXA20 reference results. The other regime is close to the constraint, is dominated by a bending behaviour and reveals ZZen-Q being more accurate than QUAD4, especially when predicting the circumferential stress.

A comparison between ZZen-Q, QUAD4, and HEXA20 results is also performed by considering the through-the-thickness distribution of both axial and circumferential stress (Figs. 12 and 13). The distribution is evaluated with the three models at $y = 11.666\ mm$, i.e., the centroid of the orange element shown in Fig. 8. When referring to the HEXA20 model, ten elements along the thickness are considered with the same y coordinate of the centroid (refer to the yellow markers of curves in Figs. 12 and 13). Since the MSC/NASTRAN QUAD4 output for stresses in multilayered shells is available at each layer mid-thickness only, in order to increase the number of available stress evaluations, the model has been modified in order to have three identical mathematical layers per each external physical layer and four identical mathematical layers within the core (refer to the orange markers of curves in Figs. 12 and 13).

Figs. 12 and 13 clearly demonstrate that ZZen-Q results are much more accurate than those obtained with QUAD4 within the external layers, with the latter model providing huge over- or under-estimations of the maximum stresses.

4.3. Application to a multilayered tank

Based on the results of the previous numerical test, we consider, as further application, the static and free vibration behaviour of a multilayered tank as obtained using only the ZZen-Q model and a high-fidelity 3D FE model. The stacking sequence is simplified but

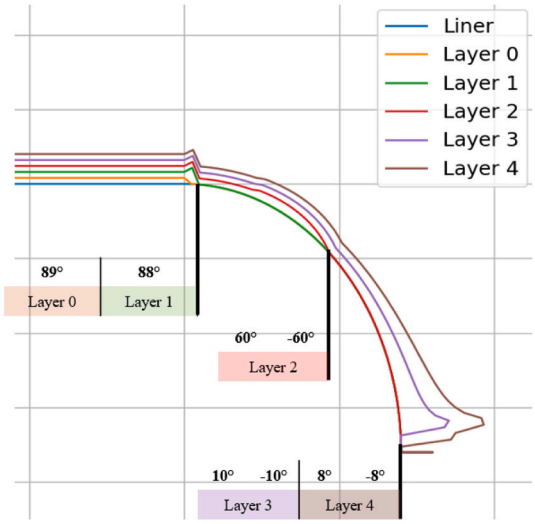


Fig. 15. Thickness distribution of the layers within the dome (Eq. (30)) with an indication of the turnaround point (the scale of the representation is magnified). Layers with orientation angles opposite in sign, have been grouped into a single layer as their turnaround points are identical.

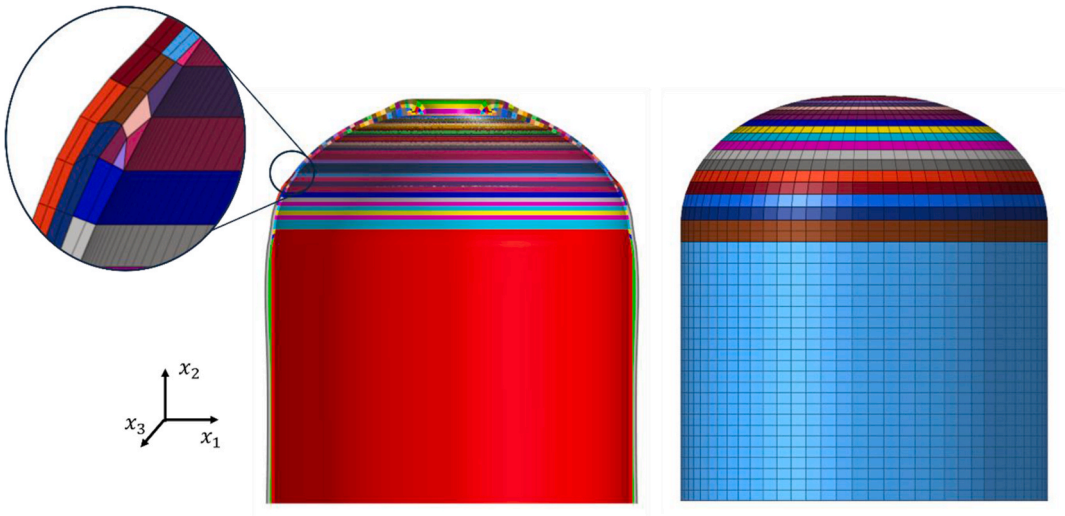


Fig. 16. Tank FE models and reference coordinate system: on the left, Abaqus 3D mesh, on the right, ZZen-Q shell mesh.

nevertheless representative of a real case (L4, refer to Table 2). The geometry of the internal liner is represented in Fig. 14 where it is shown that an elliptical dome is considered.

The L4 stacking sequence is adopted on the cylindrical part of the tank whereas, along the dome, the layer thickness and orientation vary according to a geodesic trajectory. Geodesic trajectories are assumed for the fiber deposition since the code used for generating the mesh of the ZZen-Q discretization is currently limited to geodesic paths. The introduction of a friction coefficient to account for non-geodesic trajectories is left for future developments. On the geodesic path on a surface of revolution, at any point, the radius r (distance of the point from the axis of revolution), and the angle α formed between the meridian and path direction (also representing the angle of orientation of the fibers) gradually varies according to the Clairault's equation [41–43]

$$r \cdot \sin \alpha = const \tag{28}$$

By defining the parameters r and α for the cylindrical part (R_{cyl}, α_{cyl}), we automatically define the orientation $\alpha(r)$ of the winded filament in the tank dome

$$\alpha(r) = \sin^{-1}\left(\frac{R_0}{r}\right) \tag{29}$$

Table 7
Mesh properties for the tank problem.

Model	through-the-thickness elements	elements	Total nodes	Total dofs
ZZen-Q	1	3285	3358	30222
Abaqus 3D	10	248′320	279′361	838′083

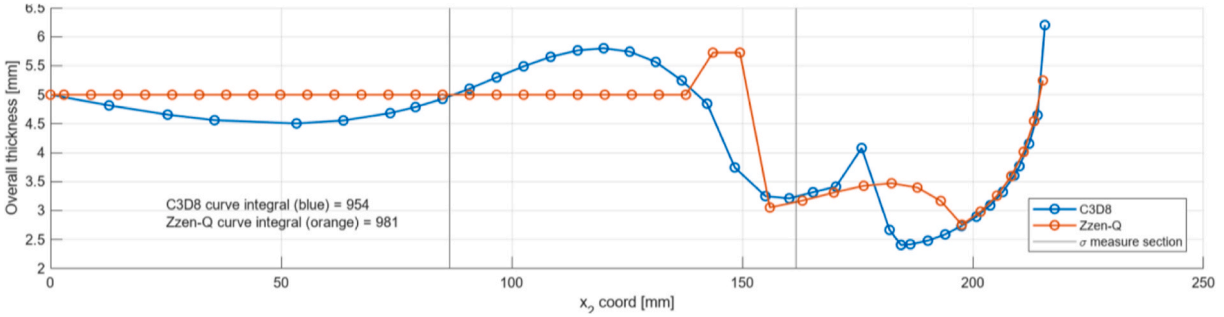


Fig. 17. Total tank thickness distribution in the Abaqus 3D and in the ZZen-Q models. The vertical lines indicate the sections selected to compare through-the-thickness stress distributions (Figs. 22–25).

Table 8
Boundary conditions for the tank static and modal analyses.

Boundary condition	Nodal DOF restrained
Symmetry with respect to the mid cross-section of the whole tank	@ $x_2 = 0 : u_2 = \theta_1 = \theta_3 = \psi_1 = \psi_3 = 0$
Reinforcing boss connection	@ $x_2 = 220 : u_1 = u_3 = \theta_2 = \psi_2 = 0$

where R_0 is the turnaround point defined as $R_0 = R_{cyl} \sin \alpha_{cyl}$. α_{cyl} are the orientation angles of the different layers of the stacking sequence (L4) in the cylindrical part of the vessel. The varying thickness $h(r)$ of the layers along the dome part is defined in Eq. (30), proposed in Ref. [44], also used in Ref. [45] and in a slightly simplified form in [46]

$$h(r) = h_{cyl} \frac{\cos \alpha_{cyl}}{\cos \alpha(r)} \frac{R_{cyl}}{r + 2BW\left(\frac{R_{cyl}-r}{R_0-r}\right)^4} \tag{30}$$

where h_{cyl} is the thickness of a specific layer in the cylindrical part of the tank and BW is the bandwidth, i.e., the width of the filament wound around the tank (here assumed to be 5 mm). Fig. 15 shows the thickness distribution of the layers within the dome as defined by Eq. (30). This distribution is approximated as a piecewise constant function in the ZZen-Q model to accompany the shell FE discretization in the dome.

The high-fidelity, reference [3D] FE model of the tank is based on Abaqus C3D8 and C3D6 elements (respectively 97.2% and 2.8% of the total number of 3D elements) and is generated using the WoundSim software [47]. A 3D FE model based on higher-order shape functions (as for the HEXA20 elements used for the cylinder in Section 4.2) would have been desirable in terms of accuracy. Nevertheless, the creation of the mesh (with associated material properties and orientations), starting from the model generated by WoundSim, would have been very difficult and the final computational effort very high. reference [3D] FE model is considered adequately accurate since (1) the presence of C3D6 elements is kept to the minimum necessary, (2) an aspect ratio <5 is guaranteed for each element in any of its three dimensions, (3) at least one element is used through-the-thickness of each material layer. Fig. 16 and Table 7 show a comparison between the shell ZZen-Q discretization and the 3D mesh. Considering Eqs. (29) and (30), both the thickness and the fiber orientation are continuously varying within the dome area. Therefore, when modeling the dome with finite elements, a discretization of these smooth variations is applied by means of the mesh scheme with several annular regions, each exhibiting a constant thickness and a constant orientation of each layer.

A careful analysis of the FE models reveals that there is a slight difference between the thicknesses reconstructed by WoundSim and those of the ZZen-Q model. These discrepancies, shown in Fig. 17, are mainly concentrated in the dome region, and originate from the different discretization approaches used by the two codes to approximate the continuously varying thickness and fiber orientations defined by Eqs. (29) and (30). In particular, the turnaround coordinates of each layer are slightly different between the two models, leading to localized thickness mismatches. Nevertheless, the thickness distribution as approximated within the ZZen-Q discretization appears to be more similar to the nominal one represented in Fig. 15. In view of the comparison between the through-the-thickness distribution of stresses as obtained by the two models, a point of the cylindrical section is selected at $x_2 = 86.5$ mm. This location has been selected because both models share the same number of layers and comparable layer thicknesses, ensuring that the through-

Table 9
Tank natural frequencies as computed with the 3D FE model, with the ZZen-Q model, and percent errors.

Mode	Abaqus 3D Frequency [Hz]	ZZen-Q Frequency [Hz]	Error [%]
f_2, f_3	1063	1056	−0.6
f_8, f_9	1514	1599	5.7
f_{14}, f_{15}	3116	2797	−10.2
f_{16}, f_{17}	3275	2857	−12.8
f_{19}, f_{20}	3457	3247	−6.1

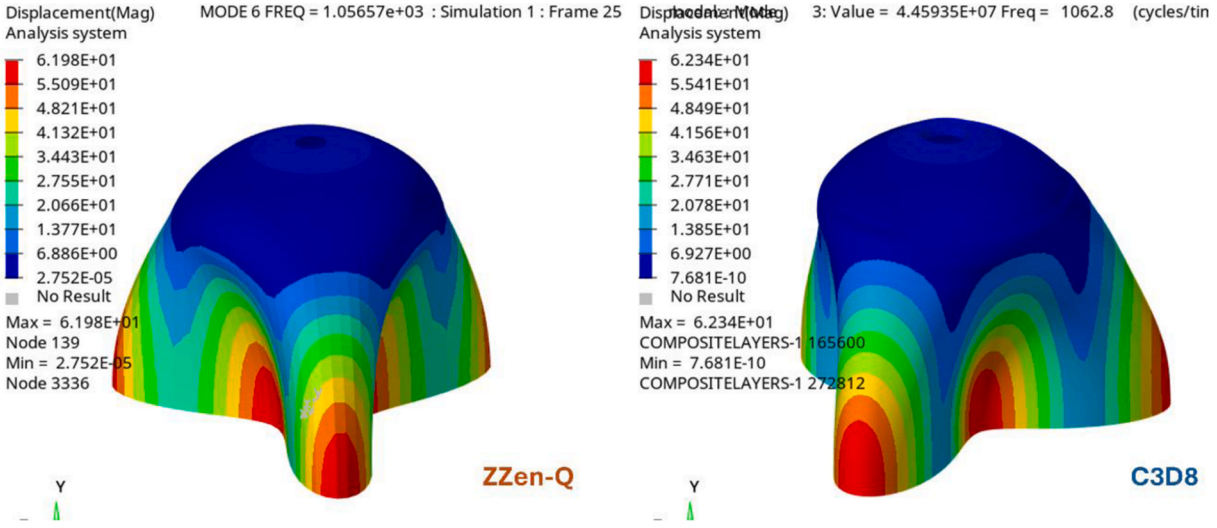


Fig. 18. Tank mode shapes f_2, f_3. ZZen-Q model on the left compared against C3D8 model on the right.

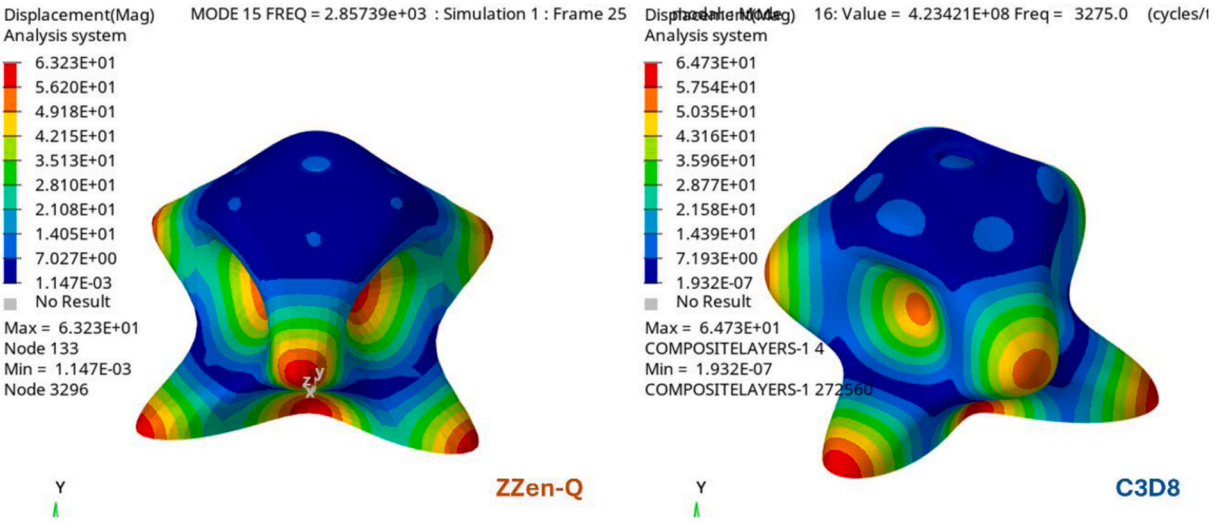


Fig. 19. Tank mode shapes f_{16}, f_{17}. ZZen-Q model on the left compared against C3D8 model on the right.

the-thickness stress comparison is performed on corresponding layers. A second section is selected at $x_2 = 161.7$ mm, located in the dome just after the turnaround points for the innermost layers (Layer 0 and 1, Fig. 15).

Half of the tank is analyzed and the boundary conditions used for both the modal and the static analysis (including the symmetry constraints) are summarized in Table 8. The lower circular edge of the analyzed models (Fig. 16, $x_2 = 0$, corresponding to the mid cross-section of the cylindrical part of the whole tank) is constrained against displacements along the x_2-axis, bending and zigzag rotations around the x_1-and x_3-axes to satisfy symmetry conditions. The top circular edge (Fig. 16, $x_2 = 220$, dome part) is constrained

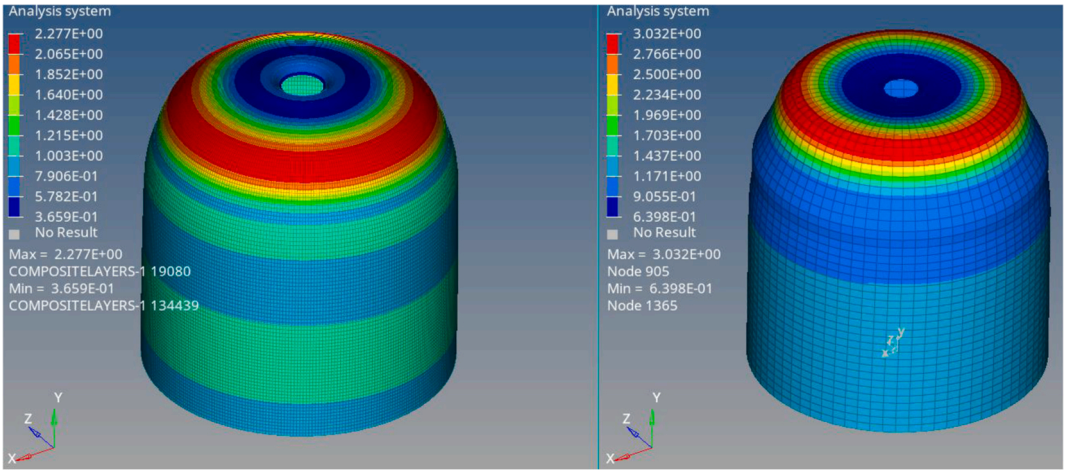


Fig. 20. Magnitude of the displacements as computed by Abaqus 3D (on the left) and ZZen-Q (on the right) for the tank subjected to internal pressure.

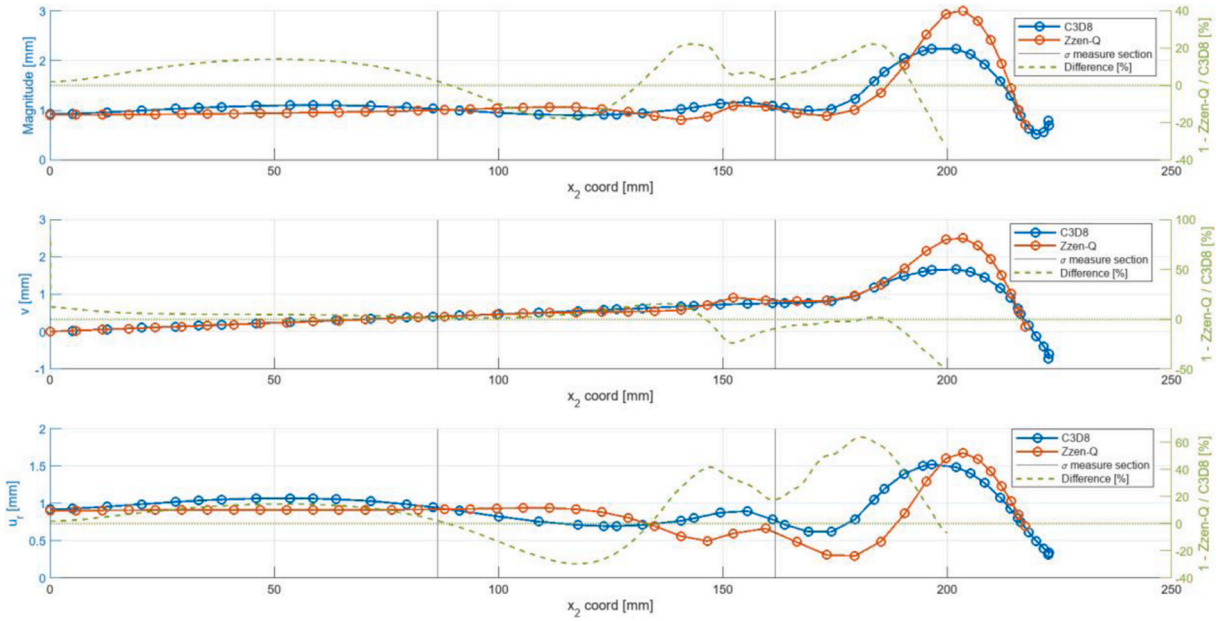


Fig. 21. Magnitude, axial and radial component of the displacements as computed by Abaqus 3D and ZZen-Q for the tank subjected to internal pressure. The percentage error of ZZen-Q with respect of Abaqus 3D is also shown. Curves are plotted for locations belonging to a meridian of the tank. The vertical lines indicate the sections selected to compare through-the-thickness stress distributions (Figs. 22–25).

against displacements along both the x_1-and the x_3-axes, and against rotations around the x_2-axis to simulate the effect of a reinforcing boss. The described constraints apply to the ZZen-Q model, whereas the Abaqus 3D model adopts those related to displacements only.

The natural frequencies reported in Table 9 are those related to the axial symmetric modes that are present in both models. The results indicate that the ZZen-Q model achieves an excellent agreement with the Abaqus 3D reference solution for the first pair of natural frequencies (corresponding to modes 2 and 3), with deviations limited to −0.6% (refer to Fig. 18 for a comparison of the mode shapes). For the intermediate modes (8 and 9) the discrepancies increase to 5.7%, while the higher-order modes (14 to 17) exhibit more substantial deviations, ranging as high as −12.8%. The increased level of discrepancy can be attributed to the more complex shapes of higher-order modes (refer to Fig. 19 showing mode shapes corresponding to frequencies f_{16} and f_{17}). Noticeably, the errors decrease again for modes 19 and 20, reaching −6.1%. Taking into account these results, ZZen-Q can be considered accurate in predicting natural frequencies of COPVs for lower modes.

A linear static analysis of the tank is also performed while maintaining the same boundary conditions (Table 8) and applying a uniform internal pressure of 35 MPa. The deformed shape of the structure is shown in Fig. 20 as obtained by the two FE models. The

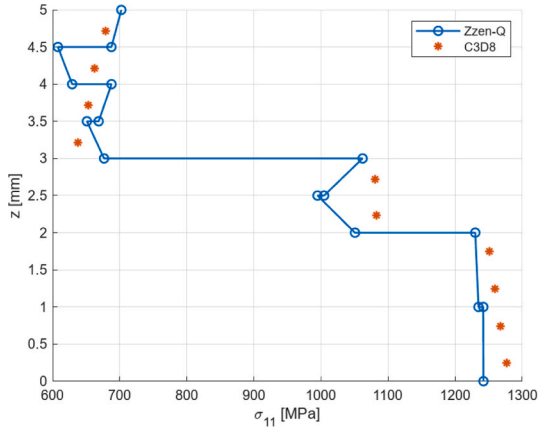


Fig. 22. Through-the-thickness distribution of the stress in fiber direction for the tank subjected to internal pressure (section $x_2 = 86.5\,mm$).

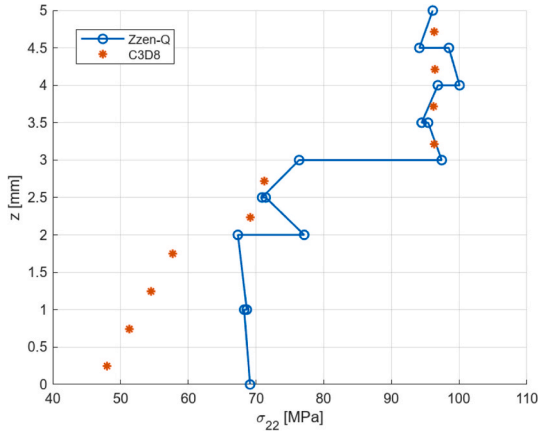


Fig. 23. Through-the-thickness distribution of the stress in matrix direction for the tank subjected to internal pressure (section $x_2 = 86.5\,mm$).

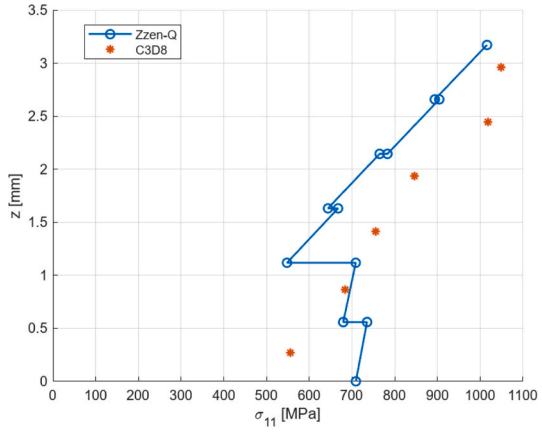


Fig. 24. Through-the-thickness distribution of the stress in fiber direction for the tank subjected to internal pressure (section $x_2 = 161.7\,mm$).

ZZen-Q model accurately reproduces the displacement field in the cylindrical region, as well as near the constraint at the dome edge. However, in the transition zone between the cylinder and the dome, the reconstruction is less accurate. Fig. 21 illustrates a qualitative trend of the displacement magnitude, of the displacement in the x_2-direction (v) and of the displacement in radial direction (u_r). The greater discrepancies between the two models in the dome region are still evident, with the larger errors likely due to the different evaluation of the thickness, as highlighted in Fig. 17. Nevertheless, the observed discrepancies remain within acceptable limits and do

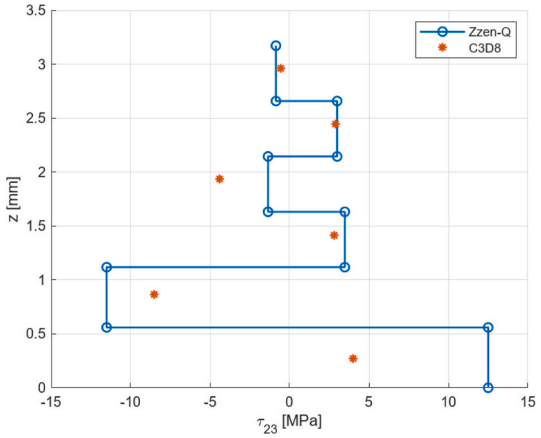


Fig. 25. Through-the-thickness distribution of the transverse shear stress in matrix-transverse direction for the tank subjected to internal pressure (section $x_2 = 161.7\ mm$).

not compromise the validity of the ZZen-Q model.

The through-the-thickness distributions shown in Figs. 22 and 23, evaluated at the section with $x_2 = 86.5\ mm$ (Fig. 17), show stresses in the fiber direction (σ_{11}) and in the matrix direction (σ_{22}). Figs. 24 and 25 report the distributions evaluated at $x_2 = 161.7\ mm$, showing the stresses in the fiber direction (σ_{11}) and the transverse shear stress in the matrix-transverse direction (τ_{23}). In all cases, coordinate $z = 0\ mm$ corresponds to the innermost interface of the composite stacking sequence, i.e. the internal surface of the tank, and increasing values of z are obtained moving outwards. At the section $x_2 = 86.5\ mm$, the agreement with the Abaqus 3D reference is particularly good in regions where stresses reach their maximum values: in the innermost layer for the fiber-direction stress and in the outermost layer for the transverse-to-fiber stress. At the section $x_2 = 161.7\ mm$, the fiber-direction stress is slightly underestimated in the outermost layers, but the overall agreement remains good. As for the transverse shear stress, τ_{23}, ZZen-Q provides an overestimated prediction in the innermost layers but correctly models the general trend.

5. Conclusions

This paper presents a novel finite element formulation based on the enhanced Refined Zigzag Theory (en-RZT) for the structural analysis of Type-IV hydrogen storage pressure vessels. The en-RZT approach is an improved version of the Refined Zigzag Theory for laminated structures that takes into account the coupled zigzag effect experienced by in-plane displacements when angle-ply stacking sequences, typical of storage pressure vessels, are considered. A quadrilateral finite element (ZZen-Q) based on the en-RZT has been therefore formulated for the first time in order to be applicable to curved structures.

A numerical investigation has been conducted in order to achieve a systematic progressive assessment of the ZZen-Q capabilities. First, convergence analyses on simply supported multilayered square plates with cross-ply and angle-ply stacking sequences have demonstrated the excellent performance of the ZZen-Q element. Compared to exact en-RZT Navier-type solutions, the element exhibits errors below 3% for both static deflections and natural frequencies, even when utilizing coarse meshes. Moreover, the analysis of a clamped sandwich cylinder subjected to internal pressure has revealed that the ZZen-Q element consistently outperforms FSDT-based, standard QUAD4 elements in providing accurate through-the-thickness distributions of stresses, in particular in bending-dominated regions near constraints and for external layers. This is achieved by ZZen-Q with a computational effort that is slightly higher than for the FSDT shell elements but is by far lower than high-fidelity, 3D FE reference solutions. Then, the analysis of a multilayered tank with a representative stacking sequence has demonstrated the practical potential of the proposed ZZen-Q approach. Despite a significantly lower computational cost (utilizing approximately 3300 elements and 30,000 DOFs), the ZZen-Q model achieves results in good agreement with a high-fidelity, 3D FE model consisting of around 250,000 elements and 840,000 DOFs. Linear modal analysis proves to be accurate for lower natural frequencies (errors below 1%), with discrepancies appearing only at higher frequencies involving complex mode shapes. Static analysis under an internal pressure confirms strong agreement for both the displacement field and through-the-thickness stress distributions within the cylindrical section. Observed discrepancies in the dome region can be attributed to differences in thickness and turnaround point discretization between the two modeling approaches, rather than inherent limitations of the en-RZT formulation.

In conclusion, the findings of this study support the en-RZT-based, ZZen-Q finite element formulation as a valuable and computationally efficient tool for the preliminary design and optimization of Composite Overwrap Pressure Vessels (COPVs). The substantial reduction in computational cost, achieved without significant loss of accuracy in primary structural quantities, enables engineers to efficiently explore several design alternatives (such as varying stacking sequences, winding angles, and layer thicknesses), prior to performing final validation with intensive 3D solid models. This computational advantage becomes increasingly significant as the number of composite layers increases; while 3D models necessitate at least one element per ply through the thickness, ZZen-Q requires only a single element, regardless of layup complexity.

Future developments of this investigation effort will focus on: (1) including thermal effects and geometric non linearities, (2) enhancing dome modeling by incorporating friction coefficients to account for non-geodesic winding paths, (3) extending the current formulation to incorporate progressive failure analysis for predicting burst pressure and failure modes under extreme loading levels, (4) integrating the ZZen-Q model into automated optimization frameworks, (5) conducting experimental validation through laboratory testing. These developments aim to further accelerate the design cycle for next-generation composite pressure vessels, supporting the infrastructure of the emerging hydrogen economy.

Declaration

During the preparation of this work, the authors used Claude (Anthropic) and Le Chat (Mistral) in order to support restructuring selected sentences to improve readability. After using these tools, the authors reviewed and edited the contents as needed and take full responsibility for the published article.

CRediT authorship contribution statement

Filippo Valoriani: Conceptualization, Data curation, Formal analysis, Investigation, Methodology, Project administration, Resources, Software, Validation, Visualization, Writing – original draft, Writing – review & editing. **Giuseppe Credo:** Formal analysis, Funding acquisition, Investigation, Software, Supervision, Validation. **Marco Gherlone:** Conceptualization, Data curation, Funding acquisition, Investigation, Methodology, Supervision, Validation, Visualization, Writing – original draft, Writing – review & editing.

Declaration of competing interest

The authors declare that they have no known competing financial interests or personal relationships that could have appeared to influence the work reported in this paper.

Acknowledgments

This publication is part of the project PNRR-NGEU (Piano Nazionale di Ripresa e Resilienza - Next Generation EU) which has received funding from the MUR (Italian Ministry of University and Research) – DM 352/2022.

Appendix A

The matrix $\boldsymbol{k}$, collecting the stiffness coefficients of the laminate according to en-RZT, is defined below

$$\boldsymbol{k} \equiv \begin{bmatrix} \mathbf{A} & \mathbf{B} & \mathbf{A}^{\phi} & \mathbf{0} & \mathbf{0} \\ \mathbf{B}^{T} & \mathbf{D} & \mathbf{B}^{\phi} & \mathbf{0} & \mathbf{0} \\ \mathbf{A}^{\phi\,T} & \mathbf{B}^{\phi\,T} & \mathbf{D}^{\phi} & \mathbf{0} & \mathbf{0} \\ \mathbf{0} & \mathbf{0} & \mathbf{0} & \mathbf{A}_t & \mathbf{B}_t \\ \mathbf{0} & \mathbf{0} & \mathbf{0} & \mathbf{B}_t^{T} & \mathbf{D}_t \end{bmatrix} \tag{A1}$$

where

$$\begin{aligned} &(\mathbf{A}, \mathbf{B}, \mathbf{D}) \equiv \langle \left(1, x_3, x_3^2\right) \boldsymbol{Q}_p^{(k)} \rangle \\ &\left(\mathbf{A}^{\phi}, \mathbf{B}^{\phi}, \mathbf{D}^{\phi}\right) \equiv \langle \left(1, x_3, \boldsymbol{\Phi}^{(k)\,T}\right) \boldsymbol{Q}_p^{(k)} \boldsymbol{\Phi}^{(k)} \rangle \\ &(\mathbf{A}_t, \mathbf{B}_t, \mathbf{D}_t) \equiv \langle \boldsymbol{Q}_t^{(k)}, \boldsymbol{Q}_t^{(k)} \boldsymbol{\beta}^{(k)}, \boldsymbol{\beta}^{(k)\,T} \boldsymbol{Q}_t^{(k)} \boldsymbol{\beta}^{(k)} \rangle \end{aligned} \tag{A2}$$

Moreover, the matrix $\boldsymbol{m}$ containing the inertia coefficients of the laminate for en-RZT has the following definition

$$\boldsymbol{m} \equiv \begin{bmatrix} m^{(0)}\mathbf{I} & 0 & m^{(1)}\mathbf{I} & \mathbf{m}_{\phi}^{(0)} \\ 0 & m^{(0)} & \mathbf{0} & \mathbf{0} \\ m^{(1)}\mathbf{I} & \mathbf{0} & m^{(2)}\mathbf{I} & \mathbf{m}_{\phi}^{(1)} \\ \mathbf{m}_{\phi}^{(0)\,T} & \mathbf{0} & \mathbf{m}_{\phi}^{(1)\,T} & \mathbf{m}_{\phi}^{(2)} \end{bmatrix} \tag{A3}$$

where

$$\begin{aligned} &\left(m^{(0)}, m^{(1)}, m^{(2)}\right) \equiv \langle \rho^{(k)} \left(1, x_3, x_3^2\right) \rangle \\ &\left(\mathbf{m}_{\phi}^{(0)}, \mathbf{m}_{\phi}^{(1)}, \mathbf{m}_{\phi}^{(2)}\right) \equiv \langle \rho^{(k)} \left(1, x_3, \boldsymbol{\phi}^{(k)\,T}\right) \boldsymbol{\phi}^{(k)} \rangle \end{aligned} \tag{A4}$$

Appendix B

The shape functions adopted for the quadrilateral elements (Eq. (14)) are $L_i(\mathbf{x})$, the isoparametric bi-linear shape functions, and the quadratic shape functions, $Q_{1i}(\mathbf{x})$ and $Q_{2i}(\mathbf{x})$, defined below

$$\left.\begin{aligned} Q_{1i}(\mathbf{x}) &\equiv \frac{1}{8}\left[P_{ki}(\mathbf{x})(x_{1i}-x_{1k})+P_{ij}(\mathbf{x})(x_{1i}-x_{1j})\right] \\ Q_{2i}(\mathbf{x}) &\equiv \frac{1}{8}\left[P_{ki}(\mathbf{x})(x_{2i}-x_{2k})+P_{ij}(\mathbf{x})(x_{2i}-x_{2j})\right] \end{aligned}\right\} \quad \begin{pmatrix} i=1,2,3,4 \\ j=2,3,4,1 \\ k=4,1,2,3 \end{pmatrix} \tag{B1}$$

with

$$\begin{aligned} P_{12}(\mathbf{x}) &\equiv \frac{1}{2}(1-\xi^2)(1-\eta) \quad P_{23}(\mathbf{x}) \equiv \frac{1}{2}(1-\eta^2)(1+\xi) \\ P_{34}(\mathbf{x}) &\equiv \frac{1}{2}(1-\xi^2)(1+\eta) \quad P_{41}(\mathbf{x}) \equiv \frac{1}{2}(1-\eta^2)(1-\xi) \end{aligned} \tag{B3}$$

and where (ξ,η) are the normalized element local in-plane coordinates, $(\xi,\eta) \in [-1,\ +1]$.

The matrix $\mathbf{N}$ containing the shape functions used for the en-RZT kinematic variables collected in the $\boldsymbol{g}$ has the following definition (Eq. (16))

$$\mathbf{N} \equiv \begin{bmatrix} [L_i] & \mathbf{0} & \mathbf{0} & \mathbf{0} & \mathbf{0} & [Q_{2i}] & \mathbf{0} & \mathbf{0} \\ \mathbf{0} & [L_i] & \mathbf{0} & \mathbf{0} & \mathbf{0} & -[Q_{1i}] & \mathbf{0} & \mathbf{0} \\ \mathbf{0} & \mathbf{0} & [L_i] & [Q_{1i}] & [Q_{2i}] & \mathbf{0} & -[Q_{1i}] & -[Q_{2i}] \\ \mathbf{0} & \mathbf{0} & \mathbf{0} & [L_i] & \mathbf{0} & \mathbf{0} & \mathbf{0} & \mathbf{0} \\ \mathbf{0} & \mathbf{0} & \mathbf{0} & \mathbf{0} & [L_i] & \mathbf{0} & \mathbf{0} & \mathbf{0} \\ \mathbf{0} & \mathbf{0} & \mathbf{0} & \mathbf{0} & \mathbf{0} & [L_i] & \mathbf{0} & \mathbf{0} \\ \mathbf{0} & \mathbf{0} & \mathbf{0} & \mathbf{0} & \mathbf{0} & \mathbf{0} & [L_i] & \mathbf{0} \\ \mathbf{0} & \mathbf{0} & \mathbf{0} & \mathbf{0} & \mathbf{0} & \mathbf{0} & \mathbf{0} & [L_i] \end{bmatrix} \tag{B4}$$

Considering the strain measures $\boldsymbol{e}$, these are related to the degrees of freedom by the following matrix (Eq. (17))

$$\mathbf{S} \equiv \begin{bmatrix} [L_{i,1}] & \mathbf{0} & \mathbf{0} & \mathbf{0} & \mathbf{0} & [Q_{2i,1}] & \mathbf{0} & \mathbf{0} \\ \mathbf{0} & [L_{i,2}] & \mathbf{0} & \mathbf{0} & \mathbf{0} & -[Q_{1i,2}] & \mathbf{0} & \mathbf{0} \\ [L_{i,2}] & [L_{i,1}] & \mathbf{0} & \mathbf{0} & \mathbf{0} & [Q_{2i,2}]-[Q_{1i,1}] & \mathbf{0} & \mathbf{0} \\ \mathbf{0} & \mathbf{0} & \mathbf{0} & [L_{i,1}] & \mathbf{0} & \mathbf{0} & \mathbf{0} & \mathbf{0} \\ \mathbf{0} & \mathbf{0} & \mathbf{0} & \mathbf{0} & [L_{i,2}] & \mathbf{0} & \mathbf{0} & \mathbf{0} \\ \mathbf{0} & \mathbf{0} & \mathbf{0} & [L_{i,2}] & [L_{i,1}] & \mathbf{0} & \mathbf{0} & \mathbf{0} \\ \mathbf{0} & \mathbf{0} & \mathbf{0} & \mathbf{0} & \mathbf{0} & \mathbf{0} & [L_{i,1}] & \mathbf{0} \\ \mathbf{0} & \mathbf{0} & \mathbf{0} & \mathbf{0} & \mathbf{0} & \mathbf{0} & \mathbf{0} & [L_{i,2}] \\ \mathbf{0} & \mathbf{0} & \mathbf{0} & \mathbf{0} & \mathbf{0} & \mathbf{0} & [L_{i,2}] & \mathbf{0} \\ \mathbf{0} & \mathbf{0} & \mathbf{0} & \mathbf{0} & \mathbf{0} & \mathbf{0} & \mathbf{0} & [L_{i,1}] \\ \mathbf{0} & \mathbf{0} & [L_{i,1}] & [L_i]+[Q_{1i,1}] & [Q_{2i,1}] & \mathbf{0} & -[Q_{1i,1}] & -[Q_{2i,1}] \\ \mathbf{0} & \mathbf{0} & [L_{i,2}] & [Q_{1i,2}] & [L_i]+[Q_{2i,2}] & \mathbf{0} & -[Q_{1i,2}] & -[Q_{2i,2}] \\ \mathbf{0} & \mathbf{0} & \mathbf{0} & \mathbf{0} & \mathbf{0} & \mathbf{0} & [L_i] & \mathbf{0} \\ \mathbf{0} & \mathbf{0} & \mathbf{0} & \mathbf{0} & \mathbf{0} & \mathbf{0} & \mathbf{0} & [L_i] \end{bmatrix} \tag{B5}$$

Appendix C

The stiffness coefficient C_ψ is defined as [28]

$$C_\psi \equiv \sqrt{\mathbf{D}_{t11}^2+\mathbf{D}_{t22}^2} \tag{C1}$$

where $\mathbf{D}_{t11}$ and $\mathbf{D}_{t22}$ are the diagonal coefficients of the matrix $\mathbf{D}_t$ (Eq. (A2)). In order to define the matrix $\widetilde{\mathbf{K}}_\psi^e$, Eq. (22) is re-written in an expanded form

$$\psi_z(\mathbf{x},t) = \mathbf{N}_\psi(\mathbf{x})\widetilde{\mathbf{q}}^e(t) \tag{C2}$$

It is obtained [28].

$$\widetilde{\mathbf{K}}_\psi^e \equiv \int_{\Omega^e} \left(\mathbf{N}_\psi{}^T\mathbf{N}_\psi - \overline{\mathbf{N}}_\psi{}^T\overline{\mathbf{N}}_\psi\right) d\Omega \tag{C3}$$

with

$$\overline{\mathbf{N}}_{\psi} \equiv \frac{1}{\Omega^e}\int_{\Omega^e} \mathbf{N}_{\psi} d\Omega \tag{C4}$$

The stiffness coefficient C_θ can be calculated as follows [28]

$$C_\theta \equiv \Omega^e \sqrt{\mathbf{A}_{t11}^2 + \mathbf{A}_{t22}^2} \tag{C5}$$

where $\mathbf{A}_{t11}$ and $\mathbf{A}_{t22}$ are the diagonal coefficients of the matrix $\mathbf{A}_t$ (Eq. (A2)). The stabilization matrix $\widetilde{\mathbf{K}}_\theta^e$ can be obtained by a summation over the 4 edges *ij* of the element (the indices *i* and *j* follow the usual cyclic permutation with $i = 1,2,3,4$ and $j = 2,3,4,1$) [28], [48]

$$\widetilde{\mathbf{K}}_\theta^e \equiv \sum_{ij} \left(\mathbf{S}_\gamma^e\right)_{ij}^T \left(\mathbf{S}_\gamma^e\right)_{ij} \tag{C6}$$

The matrix $\left(\mathbf{S}_\gamma^e\right)_{ij}$ is used to express the in-plane shear strain along each edge and at its mid-point $(\gamma_{rs})_{ij}$ in terms of the nodal degrees of freedom $\widetilde{\mathbf{q}}^e$ [28]

$$(\gamma_{rs})_{ij} = \frac{1}{\ell_{ij}^2}\left(\left(x_{1j} - x_{1i}\right)\left(v_j - v_i\right) - \left(x_{2j} - x_{2i}\right)\left(u_j - u_i\right)\right) - \frac{1}{2}\left(\theta_{zi} + \theta_{zj}\right) = \left(\mathbf{S}_\gamma^e\right)_{ij}\widetilde{\mathbf{q}}^e \tag{C7}$$

where ℓ_{ij} is the length of the edge *ij*.

Appendix D

Let us consider a point and its coordinates with respect to the element-local coordinate system, $\boldsymbol{c} = [x_1 \quad x_2 \quad x_3]^T$ (refer to Fig. 2), and with respect to the structure-global coordinate system, $\boldsymbol{C} = [X \quad Y \quad Z]^T$. The transformation from the global to the local coordinate system is

$$\boldsymbol{c} = \begin{Bmatrix} x_1 \\ x_2 \\ x_3 \end{Bmatrix} = \boldsymbol{T}\boldsymbol{C} = \begin{bmatrix} \boldsymbol{T_1} \\ \boldsymbol{T_2} \\ \boldsymbol{T_3} \end{bmatrix} \begin{Bmatrix} X \\ Y \\ Z \end{Bmatrix} \tag{D1}$$

where the row vector $\boldsymbol{T_i}$ contains the components of the local unit vector $\boldsymbol{x_i}$ with respect to the global coordinate system ($i = 1,2,3$).

The same transformation is valid for any displacement vector (from the local system, $\boldsymbol{s}$, to the global system, $\boldsymbol{S}$) and for any rotation vector (from the local system, $\boldsymbol{r}$, to the global system, $\boldsymbol{R}$) [37]

$$\boldsymbol{s} = \boldsymbol{T}\boldsymbol{S}\,\boldsymbol{r} = \boldsymbol{T}\boldsymbol{R} \tag{D2}$$

The ZZen-Q shell element has 9°-of-freedom per node in its local coordinate system, organized in a displacement vector, $\boldsymbol{s}$, and two rotation vectors, $\boldsymbol{r_\theta}$ and $\boldsymbol{r_\psi}$,

$$\boldsymbol{s} = [u_1 \quad u_2 \quad w]^T \quad \boldsymbol{r_\theta} = [\theta_1 \quad \theta_2 \quad \theta_z]^T \quad \boldsymbol{r_\psi} = [\psi_1 \quad \psi_2 \quad \psi_z]^T \tag{D3}$$

Vectors $\boldsymbol{r_\theta}$ and $\boldsymbol{r_\psi}$ are characterized by the fact that the 1st component (θ_1 and ψ_1) is a rotation around the positive x_2-axis, whereas the 2nd component (θ_2 and ψ_2) is a rotation around the negative x_1-axis. In the global coordinate system, the nodal degrees of freedom should be defined in such a way that any rotation component is in agreement with the corresponding positive global axis

$$\boldsymbol{S} = [u_X \quad u_Y \quad u_Z]^T \quad \boldsymbol{R_\theta} = [\theta_X \quad \theta_Y \quad \theta_Z]^T \quad \boldsymbol{R_\psi} = [\psi_X \quad \psi_Y \quad \psi_Z]^T \tag{D4}$$

For this reason, the transformation from the local to the global rotational degrees of freedom is modified with respect to Eq. (D2) (whereas the transformation for displacements is the same)

$$\boldsymbol{r_\theta} = \widehat{\boldsymbol{T}}\boldsymbol{R_\theta} \quad \boldsymbol{r_\psi} = \widehat{\boldsymbol{T}}\boldsymbol{R_\psi} \tag{D5}$$

where

$$\widehat{\boldsymbol{T}} = \begin{bmatrix} \boldsymbol{T_2} \\ -\boldsymbol{T_1} \\ \boldsymbol{T_3} \end{bmatrix} \tag{D6}$$

The transformation law for the set of displacement and rotation degrees of freedom of a single node of ZZen-Q will therefore be

$$\begin{Bmatrix} \boldsymbol{s} \\ \boldsymbol{r_\theta} \\ \boldsymbol{r_\psi} \end{Bmatrix} = \begin{bmatrix} \boldsymbol{T} & \boldsymbol{0} & \boldsymbol{0} \\ \boldsymbol{0} & \widehat{\boldsymbol{T}} & \boldsymbol{0} \\ \boldsymbol{0} & \boldsymbol{0} & \widehat{\boldsymbol{T}} \end{bmatrix} \begin{Bmatrix} \boldsymbol{S} \\ \boldsymbol{R_\theta} \\ \boldsymbol{R_\psi} \end{Bmatrix} \tag{D7}$$

The extension of Eq. (D7) to the complete set of degrees-of-freedom of the shell element (four nodes) is straightforward, as it is the subsequent transformation of the mass matrix, of the stiffness matrix and of the load vector from the local to the global coordinate system for final assembly and solution [37].

Data availability

Data will be made available on request.

References

[1] M. Zoghi, N. Hosseinzadeh, S. Gharaie, A. Zare, 4E comprehensive comparison and optimization of different renewable power sources for green hydrogen production, Renew. Energy 240 (Feb. 2025) 122254, https://doi.org/10.1016/j.renene.2024.122254.
[2] E. Rivard, M. Trudeau, K. Zaghib, Hydrogen storage for mobility: a review, Materials 12 (12) (Jun. 2019), https://doi.org/10.3390/ma12121973.
[3] G. Romeo, F. Danzi, E. Cestino, F. Borello, Design and optimization of a composite vessel for hydrogen storage subject to internal pressure and In-Flight loads for UAVs, Int. J. Aero. Sci. (2013).
[4] H. Yahashi, A. Yamashita, N. Shigemitsu, S. Goto, K. Kida, T. Inou, Development of high-pressure hydrogen storage system for new FCV. Presented at the SAE WCX Digital Summit, Apr. 2021, https://doi.org/10.4271/2021-01-0741, 2021-01–0741.
[5] A. Yamashita, M. Kondo, S. Goto, N. Ogami, Development of high-pressure hydrogen storage system for the Toyota "Mirai". Presented at the SAE 2015 World Congress & Exhibition, Apr. 2015, https://doi.org/10.4271/2015-01-1169, 2015-01–1169.
[6] I.A. Hassan, H.S. Ramadan, M.A. Saleh, D. Hissel, Hydrogen storage technologies for stationary and mobile applications: review, analysis and perspectives, Renew. Sustain. Energy Rev. 149 (Oct. 2021) 111311, https://doi.org/10.1016/j.rser.2021.111311.
[7] H.S. Roh, T.Q. Hua, R.K. Ahluwalia, Optimization of carbon fiber usage in Type 4 hydrogen storage tanks for fuel cell automobiles, Int. J. Hydrogen Energy 38 (29) (Sep. 2013) 12795–12802, https://doi.org/10.1016/j.ijhydene.2013.07.016.
[8] H. Barthelemy, M. Weber, F. Barbier, Hydrogen storage: recent improvements and industrial perspectives, Int. J. Hydrogen Energy 42 (11) (Mar. 2017) 7254–7262, https://doi.org/10.1016/j.ijhydene.2016.03.178.
[9] S.T. Peters (Ed.), Composite Filament Winding, ASM International, Materials Park, Ohio, 2011.
[10] NASA, 'Making a Metal-Lined Composite-Overwrapped Pressure Vessel The metal liner reduces loss of gas by diffusion without adding much weight.' marshall space flight center, Alabama. Accessed: March. 10, 2026. [Online]. Available: https://ntrs.nasa.gov/api/citations/20110014768/downloads/20110014768.pdf.
[11] P. O. of the E. Union, 'Regulation No 134 of the Economic Commission for Europe of the United Nations (UN/ECE) — uniform provisions concerning the approval of motor vehicles and their components with regard to the safety-related performance of hydrogen-fuelled vehicles (HFCV) [2019/795]', Publications Office of the EU. Accessed: April. 2, 2026. [Online]. Available: https://op.europa.eu/en/publication-detail/-/publication/8aad3d19-7870-11e9-9f05-01aa75ed71a1.
[12] M. Nebe, A. Soriano, C. Braun, P. Middendorf, F. Walther, Analysis on the mechanical response of composite pressure vessels during internal pressure loading: FE modeling and experimental correlation, Compos. B Eng. 212 (May 2021) 108550, https://doi.org/10.1016/j.compositesb.2020.108550.
[13] M. Nebe, A. Johman, C. Braun, J.M.J.F. Van Campen, The effect of stacking sequence and circumferential ply drop locations on the mechanical response of type IV composite pressure vessels subjected to internal pressure: a numerical and experimental study, Compos. Struct. 294 (Aug. 2022) 115585, https://doi.org/10.1016/j.compstruct.2022.115585.
[14] W. Li, et al., Reliability analysis of hydrogen storage composite pressure vessel with two types of random-interval uncertainties, Int. J. Hydrogen Energy 48 (81) (Sep. 2023) 31685–31699, https://doi.org/10.1016/j.ijhydene.2023.04.312.
[15] Q. Wang, et al., Failure prediction and optimization for composite pressure vessel combining FEM simulation and machine learning approach, Compos. Struct. 337 (Jun. 2024) 118099, https://doi.org/10.1016/j.compstruct.2024.118099.
[16] E. Reissner, Y. Stavsky, Bending and stretching of certain types of heterogeneous aeolotropic elastic plates, J. Appl. Mech. 28 (3) (Sep. 1961) 402–408, https://doi.org/10.1115/1.3641719.
[17] E. Reissner, The effect of transverse shear deformation on the bending of elastic plates, J. Appl. Mech. 12 (2) (Jun. 1945) A69–A77, https://doi.org/10.1115/1.4009435.
[18] R.D. Mindlin, Influence of rotatory inertia and shear on flexural motions of isotropic, elastic plates, J. Appl. Mech. 18 (1) (Mar. 1951) 31–38, https://doi.org/10.1115/1.4010217.
[19] S. Abrate, M. Di Sciuva, Equivalent single layer theories for composite and sandwich structures: a review, Compos. Struct. 179 (Nov. 2017) 482–494, https://doi.org/10.1016/j.compstruct.2017.07.090.
[20] K.M. Liew, Z.Z. Pan, L.W. Zhang, An overview of layerwise theories for composite laminates and structures: development, numerical implementation and application, Compos. Struct. 216 (May 2019) 240–259, https://doi.org/10.1016/j.compstruct.2019.02.074.
[21] J.M. Whitney, The effect of transverse shear deformation on the bending of laminated plates, J. Compos. Mater. 3 (3) (Mar. 1969) 534–547, https://doi.org/10.1177/002199836900300316.
[22] H. Murakami, Laminated composite plate theory with improved In-Plane responses, J. Appl. Mech. 53 (3) (Sep. 1986) 661–666, https://doi.org/10.1115/1.3171828.
[23] M. Di Sciuva, Development of an anisotropic, multilayered, shear-deformable rectangular plate element, Comput. Struct. 21 (4) (1985) 789–796, https://doi.org/10.1016/0045-7949(85)90155-5.
[24] M. Cho, R.R. Parmerter, An efficient higher-order plate theory for laminated composites, Compos. Struct. 20 (2) (Jan. 1992) 113–123, https://doi.org/10.1016/0263-8223(92)90067-M.
[25] A. Tessler, M. Di Sciuva, M. Gherlone, A consistent refinement of first-order shear deformation theory for laminated composite and sandwich plates using improved zigzag kinematics, J. Mech. Mater. Struct. 5 (2) (Aug. 2010) 341–367, https://doi.org/10.2140/jomms.2010.5.341.
[26] A. Tessler, M. Di Sciuva, M. Gherlone, A homogeneous limit methodology and refinements of computationally efficient zigzag theory for homogeneous, laminated composite, and sandwich plates, Numerical Methods Partial 27 (1) (Jan. 2011) 208–229, https://doi.org/10.1002/num.20646.
[27] M. Gherlone, On the use of zigzag functions in equivalent single layer theories for laminated composite and sandwich beams: a comparative study and some observations on external weak layers, J. Appl. Mech. 80 (6) (Nov. 2013) 061004, https://doi.org/10.1115/1.4023690.
[28] M. Gherlone, D. Versino, V. Zarra, Multilayered triangular and quadrilateral flat shell elements based on the Refined Zigzag Theory, Compos. Struct. 233 (Feb. 2020) 111629, https://doi.org/10.1016/j.compstruct.2019.111629.
[29] L. Iurlaro, M. Gherlone, M. Di Sciuva, A. Tessler, Refined Zigzag Theory for laminated composite and sandwich plates derived from Reissner's Mixed Variational Theorem, Compos. Struct. 133 (Dec. 2015) 809–817, https://doi.org/10.1016/j.compstruct.2015.08.004.
[30] A. Kutlu, M. Dorduncu, T. Rabczuk, A novel mixed finite element formulation based on the Refined Zigzag Theory for the stress analysis of laminated composite plates, Compos. Struct. 267 (Jul. 2021) 113886, https://doi.org/10.1016/j.compstruct.2021.113886.
[31] A. Barut, E. Madenci, A. Tessler, C0-continuous triangular plate element for laminated composite and sandwich plates using the {2, 2} – Refined Zigzag Theory, Compos. Struct. 106 (Dec. 2013) 835–853, https://doi.org/10.1016/j.compstruct.2013.07.024.

[32] M. Dorduncu, A. Kutlu, E. Madenci, Triangular C0 continuous finite elements based on Refined Zigzag Theory {2,2} for free and forced vibration analyses of laminated plates, Compos. Struct. 281 (Feb. 2022) 115058, https://doi.org/10.1016/j.compstruct.2021.115058.
[33] L. Iurlaro, M. Gherlone, M. Di Sciuva, The (3,2)-Mixed Refined Zigzag Theory for generally laminated beams: theoretical development and C0 finite element formulation, Int. J. Solid Struct. 73–74 (Nov. 2015) 1–19, https://doi.org/10.1016/j.ijsolstr.2015.07.028.
[34] M. Sorrenti, M. Di Sciuva, An enhancement of the warping shear functions of Refined Zigzag Theory, J. Appl. Mech. 88 (8) (Aug. 2021) 084501, https://doi.org/10.1115/1.4050908.
[35] M. Sorrenti, M. Gherlone, Robust TRIA3 and QUAD4 finite elements based on the En-Rzt kinematics for the analysis of general anisotropic multilayered composite plates, Mech. Compos. Mater. 60 (5) (Nov. 2024) 1001–1026, https://doi.org/10.1007/s11029-024-10241-y.
[36] G. Wei, P. Lardeur, F. Druesne, Solid-shell approach based on first-order or higher-order plate and shell theories for the finite element analysis of thin to very thick structures, Eur. J. Mech. Solid. 94 (Jul. 2022) 104591, https://doi.org/10.1016/j.euromechsol.2022.104591.
[37] O.C. Zienkiewicz, R.L. Taylor, J.Z. Zhu, The Finite Element Method: Its Basis and Fundamentals, Butterworth-Heinemann, 2013, https://doi.org/10.1016/C2009-0-24909-9.
[38] A. Tessler, Comparison of interdependent interpolations for membrane and bending kinematics in shear-deformable shell elements, in: Proceedings of International Conference on Computational Engineering and Sciences, 2000. *Los Angeles, CA*.
[39] A. Tessler, J. Mohr, A three-node shell element with drilling degrees of freedom for laminated composite and sandwich structures, in: Fourth International Colloquium on Computation of Shell & Spatial Structures, Chania, Crete, Greece, 2000.
[40] A. Tessler, S.B. Dong, On a hierarchy of conforming timoshenko beam elements, Comput. Struct. 14 (3) (1981) 335–344, https://doi.org/10.1016/0045-7949(81)90017-1.
[41] Sotiris Koussios, Filament winding: a unified approach, DUP Science (2004) [Online]. Available: https://resolver.tudelft.nl/uuid:41b62a9a-c15e-4026-b600-66ca4701941c.
[42] Wongvisarut Khuangsatung, Pakkinee Chitsakul, Some Geodesics in Open Surfaces Classified by Clairaut, S Relation', Sep. 2012, https://doi.org/10.5281/ZENODO.1070305.
[43] I.H. Dalibor, T.V. Lisbôa, R.J. Marczak, S.C. Amico, Optimum slippage dependent, non-geodesic fiber path determination for a filament wound composite nozzle, Eur. J. Mech. Solid. 82 (Jul. 2020) 103994, https://doi.org/10.1016/j.euromechsol.2020.103994.
[44] A.A. Krikanov, Refined thickness of filament wound shells, Sci. Eng. Compos. Mater. 10 (4) (Aug. 2002) 241–248, https://doi.org/10.1515/SECM.2002.10.4.241.
[45] J.P. Berro Ramirez, D. Halm, J.-C. Grandidier, S. Villalonga, F. Nony, 700 bar type IV high pressure hydrogen storage vessel burst – simulation and experimental validation, Int. J. Hydrogen Energy 40 (38) (Oct. 2015) 13183–13192, https://doi.org/10.1016/j.ijhydene.2015.05.126.
[46] L. Zu, S. Koussios, A. Beukers, Shape optimization of filament wound articulated pressure vessels based on non-geodesic trajectories, Compos. Struct. 92 (2) (Jan. 2010) 339–346, https://doi.org/10.1016/j.compstruct.2009.08.013.
[47] S VERTICAL, Woundsim Documentation, Feb. 11, 2026. S VERTICAL, https://www.svertical.com/file-share. (Accessed 11 February 2026).
[48] J.W. Mohr, An Efficient Triangular Shell Finite Element for Thick Composite and Sandwich Laminates, George Washington University, 2000. PhD Thesis.